



저작자표시-비영리-변경금지 2.0 대한민국

이용자는 아래의 조건을 따르는 경우에 한하여 자유롭게

- 이 저작물을 복제, 배포, 전송, 전시, 공연 및 방송할 수 있습니다.

다음과 같은 조건을 따라야 합니다:



저작자표시. 귀하는 원저작자를 표시하여야 합니다.



비영리. 귀하는 이 저작물을 영리 목적으로 이용할 수 없습니다.



변경금지. 귀하는 이 저작물을 개작, 변형 또는 가공할 수 없습니다.

- 귀하는, 이 저작물의 재이용이나 배포의 경우, 이 저작물에 적용된 이용허락조건을 명확하게 나타내어야 합니다.
- 저작권자로부터 별도의 허가를 받으면 이러한 조건들은 적용되지 않습니다.

저작권법에 따른 이용자의 권리는 위의 내용에 의하여 영향을 받지 않습니다.

이것은 [이용허락규약\(Legal Code\)](#)을 이해하기 쉽게 요약한 것입니다.

[Disclaimer](#)

이학박사 학위논문

Experimental Study on
Highly Electrically Conductive
Reduced Graphene Oxide Free-standing Film

높은 전기전도성을 가지는
독립된 환원그래핀옥사이드 필름 개발에 대한 연구

2021년 2월

서울대학교 대학원

물리천문학부

홍 동 표

이학박사 학위논문

Experimental Study on
Highly Electrically Conductive
Reduced Graphene Oxide Free-standing Film

높은 전기전도성을 가지는
독립된 환원그래핀옥사이드 필름 개발에 대한 연구

2021년 2월

서울대학교 대학원

물리천문학부

홍 동 표

Experimental Study on
Highly Electrically Conductive
Reduced Graphene Oxide Free-standing Film

높은 전기전도성을 가지는
독립된 환원그래핀옥사이드 필름 개발에 대한 연구
지도교수 박 건 식

이 논문을 이학박사 학위논문으로 제출함

2021년 1월

서울대학교 대학원

물리천문학부

홍 동 표

홍동표의 박사 학위논문을 인준함

2021년 1월

위 원 장	김 기 훈	
부 위 원 장	박 건 식	
위 원	박 윤	
위 원	박 철 환	
위 원	박 상 윤	

Abstract

Dongpyo Hong

Department of physics and astronomy

The Graduate school

Seoul National University

In this study, the correlation between the structure and electrical properties of the reduced graphene oxide (rGO) free-standing film was experimentally investigated, and a facile synthesis method for the rGO film with record-high electrical conductivity and record-high carrier mobility was proposed. Despite the continuing need for the highly electrically conductive carbon-based free-standing film for the realization of flexible electronics, the electrical conductivity of the existing rGO free-standing film is limited to be below that of highly ordered pyrolytic graphite. This bottleneck arises from the trade-off between the removal of in-plane defects and the accompanying graphitization in the structural restoration process. In other words, thermal rearrangement of carbon in rGO film at high-temperature not only eliminates the oxygen and in-plane defects but also transform the turbostratic stacking region into the AB-stacking region, which limits the electronic band structure of rGO film to be parabolic even when in-plane crystallinity is highly restored.

Here, macroscopic graphene film with record-high electrical conductivity ($1.95 \times 10^6 \text{ S m}^{-1}$) and mobility ($720 \text{ cm}^2 \text{ V}^{-1} \text{ s}^{-1}$) is reported. The resulting reduced graphene oxide (rGO) freestanding film shows highly restored in-plane crystallinity while turbostratic stacking order is almost retained. The film is prepared by mild annealing of binder-free graphene oxide (GO)

hydrogel film at 1800°C. The portion of the AB-stacking region was controlled via rational engineering of GO film precursor by sonication-assisted gelation without any additives. A two-fold mechanism of regulation is proposed in this study: the removal of unexfoliated graphite oxide and the limitation of relative rearrangement of GO nanosheets by cross-linking formation in GO hydrogel.

Here it is also revealed that the excellent electrical properties of the rGO film are attributed to the optimization of the interplay between stacking order and degree of defect. By investigating the stacking order, defects, and electronic properties of the rGO film according to the state of GO precursor, we experimentally confirmed for the first time that the electrical properties of the rGO film are largely dependent on the stacking order in a low-defect regime. Therefore, this research not only suggests a cost-effective, green, scalable synthesis method for ultrahigh electrically conductive free-standing graphene film but also propose the direction of future development to transfer the superior properties of ideal graphene into macroscopic rGO film.

Keywords: graphene, graphene oxide, reduced graphene oxide, free-standing film, hydrogel, electrical conductivity, carrier mobility, defect, stacking order

Student number: 2014-21342

Contents

Abstaract.....	1
Chapter 1 Introduction	10
1.1 Graphene	10
1.2 Graphene oxide and reduced graphene oxide	11
1.3 Reduced graphene oxide film.....	14
1.4 Electrical properties of graphene-based macroscopic film	15
1.5 Previous efforts to improve electrical conductivity of rGO free-standing film	19
Chapter 2 Aims and Motivations	27
2.1 Objectives and Scopes	27
2.2 Hypothesis.....	28
Chapter 3 Method & Materials.....	31
3.1 GO Synthesis, GO hydrogel synthesis	31
3.2 GO, rGO film synthesis	32

3.3	Electrical conductivity measurements.....	37
3.4	Raman spectroscopy	44
3.5	X-ray diffraction	47
3.6	X-ray photoelectron spectroscopy.....	48
Chapter 4 Tailoring the electrical properties of rGO film by structural engineering		50
4.1	Various phase of GO dispersion	50
4.2	Structural evolution of GO hydrogel during sonication.....	51
4.3	Thermal deoxygenation and restoration of rGO film.....	58
4.4	Engineering of stacking order via precursor engineering	70
4.5	Stacking-order driven electrical properties of rGO film	79
4.6	Thermal expansion assisted hot pressing	85
Chapter 5 Summary and Conclusion		88
Bibliography.....		89

List of Figures

Figure 1.2.1 Aberration corrected TEM images of the single suspended sheet of GO ¹⁵	12
Figure 1.2.2 Atomic structure of reduced graphene oxide sheet ¹⁶	13
Figure 1.4.1 Schematic for carrier scattering path in the material ³⁶	16
Figure 1.4.2 Electrical conductivity of thermally reduced GO as a function of the sp ² carbon fraction ³⁷	17
Figure 1.4.3 band structure of multilayer graphene depending on the stacking order	18
Figure 1.5.1 Structural defects limiting the electrical properties of rGO film	19
Figure 1.5.2 Previous works on improving the electrical conductivity of rGO film	20
Figure 1.5.3 Applications of highly electrically conductive, flexible free-standing film	21
Figure 1.5.4 Previous efforts to synthesize the turbostratic stacking multilayer graphene ⁴¹	24
Figure 2.2.1 Rotational diffusion of a graphene flake on a graphene layer ⁷⁵	28

Figure 2.2.2 hypothesis on the regulation of stacking order by engineering GO precursor	29
Figure 3.2.1 Fabrication process of free-standing graphene film from GO hydrogel	32
Figure 3.2.2 Digital photograph for GO hydrogel coating process	33
Figure 3.2.3 Digital photograph and optical microscope image for GO film after detachment	33
Figure 3.2.4 Stress-strain curve and cross-section of GO film.....	34
Figure 3.2.5 Top view surface of rGO film before and after mechanical pressing.....	35
Figure 3.2.6 Digital photograph and cross-section SEM image of rGO film	36
Figure 3.3.1 Typical 4-point probe equipment and schematic for operation principle	37
Figure 3.3.2 Two-terminal (a) and four-terminal (b) resistance measurement conceptual diagram.....	38
Figure 3.3.3 Current flow and voltage measurement of the 1-point probe (a), 2-point probe (b), and collinear 4-point probe (c).....	39
Figure 3.3.4 Approximation of thickness correction factor.....	42
Figure 3.3.5 Repeated sheet resistance measurement by the 4-probe method	43
Figure 3.4.1 Working principle of Raman spectroscopy	44

Figure 3.4.2 Raman spectroscopy equipment used in this study.....	45
Figure 3.5.1 X-ray diffraction equipment used in this study.....	47
Figure 3.6.1 Working principle of X-ray photoelectron spectroscopy	48
Figure 3.6.2 Principle of X-ray photoelectron spectroscopy.....	49
Figure 4.1.1 Various arrested states of GO dispersion ⁷⁸	51
Figure 4.2.1 Degree of exfoliation with varying sonication time measured by WAXS.....	52
Figure 4.2.2 SEM images of drop cast graphene oxide nanosheets on SiO ₂ wafer with different sonication time.....	53
Figure 4.2.3 Viscosity and sheet size depending on the sonication time.....	54
Figure 4.2.4 SEM images lyophilized hydrogels sonicated for the different time	55
Figure 4.2.5 SAXS 2D pattern of the GO hydrogel sonicated for a different time	56
Figure 4.3.1 XPS spectra of graphene oxide film	58
Figure 4.3.2 (a)C 1s and (b)O 1s peak in XPS spectra of the graphene oxide film	59
Figure 4.3.3 (a)S 2p, (b)K 2p, and (c)Mn 2p _{3/2} peaks.....	60
Figure 4.3.4 XPS wide scan with varying sonication time.....	61
Figure 4.3.5 C/O ratio calculated from XPS analysis depending on the sonication time.....	62

Figure 4.3.6 XPS wide scan spectra(a) and C1s peak (b).....	63
Figure 4.3.7 Oxygen contents of rGO film annealed at different temperature	64
Figure 4.3.8 absence of S 2p peak in XPS spectra of 1800°C annealed rGO film	65
Figure 4.3.9 Raman spectra from GO and rGO film annealed at various temperatures.....	65
Figure 4.3.10 Deconvolution of D and G peak in Raman spectra of GO(a) and rGO film annealed at 600°C (b) 1200°C (c) and 1800°C (d).....	67
Figure 4.3.11 Deconvolution of Raman 2D peak.....	68
Figure 4.3.12 Graphitic portion, degree of defect, and oxygen percentage of rGO film depending on the annealing temperature	69
Figure 4.4.1 Raman spectra(a) and 2D peak deconvolution(b) with varying sonication time of GO precursor	72
Figure 4.4.2 Center position and FWHM of Raman 2D peak depending on the sonication time.....	74
Figure 4.4.3 Comparison of adjusted R-square value of single peak fitting and triple peak fitting	74
Figure 4.4.4 Deconvolution of the X-ray diffraction pattern from rGO film with varying sonication time	75
Figure 4.4.5 Degree of the defect and graphitic portion of rGO film depending on the sonication period of GO hydrogel	76
Figure 4.4.6 TEM images and selected area electron diffraction pattern of	

rGO flake from rGO film (90 min, 1800°C). AB-stacking region (a), turbostratic stacking region (b), (c).77

Figure 4.5.1 Maximization of electrical properties by an interplay between defect and stacking order (a) in-plane electrical conductivity of rGO film with varying sonication time of GO hydrogel measured by Van der Pauw method. (b) the in-plane carrier mobility of rGO film with varying sonication time of GO hydrogel measured by Hall measurement system. (c) Inverse product of $2D_2/(2D_2 + 2DT)$ and ID/IG depending on the sonication time of GO hydrogel were calculated from Figure 2e. Range of optimized conductivity, mobility, and structural parameters are marked as a shaded region. Gray circles in (a) and (b) represent each sample measurements with an errorbar denoting standard deviation of three independent measurements79

Figure 4.5.2 Linear correlation between mobility and conductivity81

Figure 4.5.3 Comparison of electrical conductivity and mobility with previous researches82

Figure 4.6.1 Designed hot press jig based on W and graphite. Thickness depending on the pressure and heating rate. Electrical conductivity depending on pressure at 1800°C annealing. Optical and SEM image with different pressing conditions85

Figure 4.6.2 Raman spectra of graphene film with different annealing temperature and pressure86

Chapter 1

Introduction

1.1 Graphene

Graphene is a two-dimensional (2D) sheet with a honeycomb lattice, which is composed solely of sp² hybridized carbon atoms. Theoretically, graphene has been studied for more than seventy years, and graphene was suggested as a concept of an building block of 3D carbon-based materials.¹ Until the recent two decades, graphene was considered to be unable to self-sustain and thus studied only theoretically as academic material. However, in 2004 Andre Geim and Konstantin Novoselov succeeded in separating stable single-layer graphene from natural graphite by the micromechanical cleavage.² Numerous studies of graphene properties following the discovery have revealed unprecedentedly excellent properties of graphene such as high electrical conductivity ($\sim 10^8$ S/m), excellent mechanical strength (~ 130 GPa), and exceptional thermal conductivity (~ 5000 W m⁻¹ K⁻¹).^{2,3} In particular, graphene's ultrahigh intrinsic mobility ($2 * 10^5$ cm²V⁻¹s⁻¹) at room temperature suggests great potential for electronic device applications providing a performance breakthrough.⁴ It has been expected that the combination of various additional advantages such as chemical and thermal stability, transparency, high surface area, lightweight, and flexibility enables the replacement of existing materials in various applications into graphene-

based materials. Indeed, numerous researches proved that performance breakthrough using graphene is possible in various devices such as flexible display, touch screen, flexible transistor, wearable devices, wideband-ultrafast photodetector, etc.⁵⁻⁷

The synthesis of high-quality, large-area graphene has been pursued in various ways such as mechanical exfoliation techniques, chemical vapor deposition, epitaxial growth, solution-phase exfoliation, and unzipping of a carbon nanotube.⁸ While the bottom-up approaches had limitations in terms of scalability and productivity, top-down approach such as graphene oxide nanosheets that can be synthesized through chemical exfoliation from graphite abundant in nature have great advantages in terms of mass production and scalability.⁹ Furthermore, graphene oxide nanosheets can form stable aqueous dispersions, so they can be easily processed and converted into reduced graphene oxide through a series of reduction processes.¹⁰

1.2 Graphene oxide and reduced graphene oxide

Graphene oxide can be synthesized through several methods, among them, nowadays modified Hummer's method is most widely used as the most efficient method considering the synthesis time and hazardousness.^{11,12} GO has a structure of hexagonal carbon lattice decorated with hydroxyl, epoxy, carbonyl, and carboxyl group.^{13,14} Although the exact configuration of GO nanosheet including sheet size and chemical composition is depending on the reaction conditions, typically GO consists of about 50-80 atomic % carbon. Along with the oxygen functional groups, structural defect such as vacancy

or topological defects within the hexagonal σ framework of carbon skeleton easily form during the oxidation process. Epoxy group and carbonyl groups exist mainly on the basal plane while the edge of the nanosheet is terminated by carboxyl and hydroxyl groups. The edge termination groups are known to be ionized readily in water, which makes graphene oxide possess a negative net charge. This negative net charge induces the strong repulsion between GO nanosheets, which ensures the stable aqueous dispersion of graphene oxide.¹⁵ More specifically, Dan Li et al. reveal the mechanism of stabilization of GO nanosheets inside the water. They demonstrated that graphene oxide sheets are highly negatively charged when dispersed in water, because of ionized carboxylic acid and hydroxyl groups that are known to exist on the GO sheets edge. From these results, they conclude that the high dispersibility of graphene oxide in aqueous colloid should be attributed to electrostatic repulsion, rather than just the hydrophilic interaction.

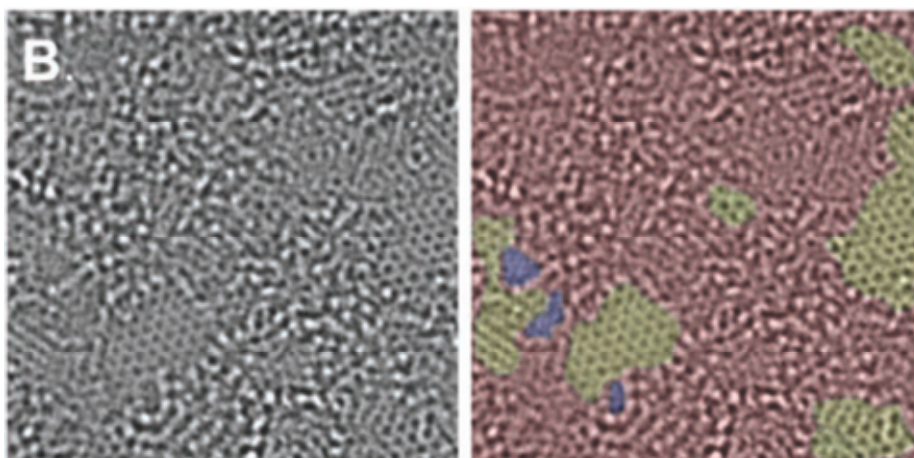


Figure 1.2.1 Atomic structure of graphene oxide imaged by transmission electron microscope¹⁶

Despite the advantage of the oxygen functional groups on processibility, lots

of functional groups and structural defects formed during the oxidation process inside the GO sheets are detrimental to its physical properties such as mechanical strength, thermal conductivity, and electrical conductivity. Indeed, graphene oxide is an insulator because these discontinuities act as a scattering origin for electrons traveling through the graphene oxide. Therefore, an appropriate reduction process depending on the application should be followed.

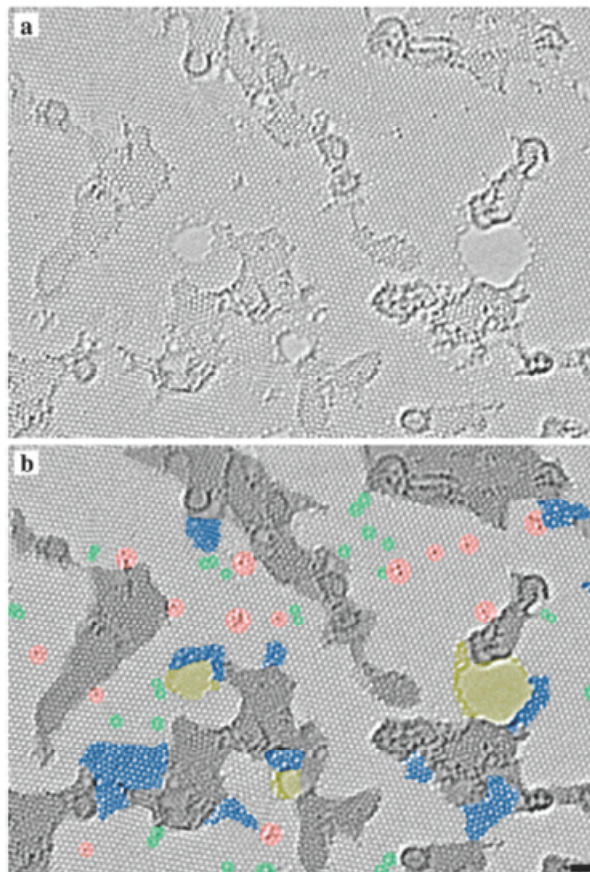


Figure 1.2.2 Atomic structure of reduced graphene oxide sheet ¹⁷

Many reduction techniques are proposed in the last decades. ^{18,19} These approaches can be categorized by mainly chemical reduction, thermal

reduction, photoreduction, and a combination of that. In the case of chemical reduction, recently, hydrazine and HI reduction are most widely used in terms of effectiveness.^{15,20} However, since chemical reduction agents are effective only for specific functional groups, there is a limitation in reducing the oxygen level of the film to a certain extent (>10 %). To completely remove oxygen from rGO sheet or rGO-based macroscopic material, high-temperature annealing of over 1200°C is accepted as the most effective method. Moreover, even if the oxygen group is removed, there are numerous structural defects remaining, so carbon rearrangement through high-temperature heating over 1500 degree is essential to achieve the highest level of physical properties.

1.3 Reduced graphene oxide film

The development of mechanically robust and highly electrically conductive free-standing films are in great demand for the diverse applications, including electromagnetic interference shielding material, and electrode for the ultrafast electronics, energy devices and sensors^{10,21-24}. The outstanding properties of monolayer pristine graphene raised expectations for the use of graphene-based free-standing film on these applications. The recently emerged macroscopic graphene film are promising alternative for the metallic conductors because of its flexibility, chemical and thermal stability²⁵⁻³⁰. Graphene oxide (GO) is a most common precursor for the mass-production of graphene films, because it can be obtained has good solution processability, and can be readily prepared via cost-effective chemical approaches with high yields^{15,31,32}. Advanced techniques have been developed to fabricate large area graphene films from graphene oxide aqueous solution, such as electrospray deposition integrated with a continuous roll-to-roll process²⁶

wet-spinning,³³ gel-film transformations³⁴, and continuous centrifugal casting^{35,36} mainly based on random overlapping of graphene oxide nanosheets, which is followed by an appropriate reduction technique.

1.4 Electrical properties of graphene-based macroscopic film

In the frame of the semi-classical Drude model, the electrical conductivity of the material is determined by the product of carrier mobility and carrier density.

$$\sigma = ne\mu$$

The carrier charge density depends on three-dimensional density states for semiconductors, and the number of valence electrons and material density for metals. Usually, this material-based property can be manipulated by doping with other materials. On the other hand, the mobility represent how fast the electrons (holes) can move through the material under the applied electric field across the material.

$$v_d = \mu E$$

The mobility of the material can be altered a lot by impurities density, defect density and temperature. Along with the effective mass, scattering time is the main factor determining the mobility, where the electrons are assumed to be ballistically transported within this scattering time until it colloid.

$$\mu = e\tau/m^*$$

The origin of scattering in material can be diverse including impurities, defect and thermal vibration of lattice. Here, defect means any structure

causing non-perfect hexagonal lattice including dislocations, grain boundaries, vacancies, and topological defects.

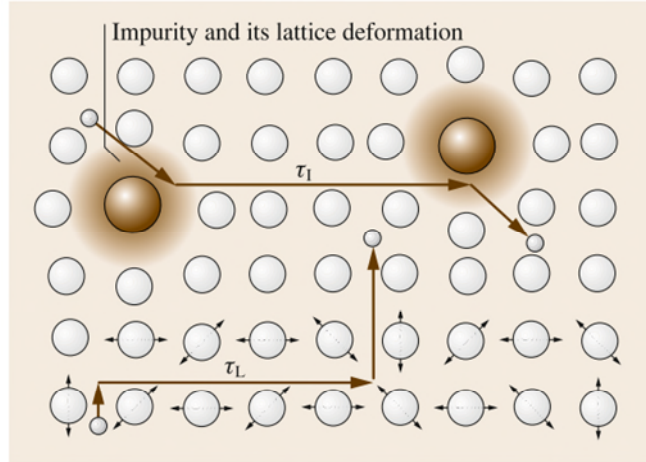


Figure 1.4.1 Schematic for carrier scattering path in the material ³⁷

The electron travelling through the material with periodic lattice structure experiences various scattering from impurities or lattice vibrations as shown in figure 1.4.1. ³⁷ Here the two mean free times τ_L and τ_I are defined: τ_L is the time interval of scattering originated from lattice vibrations (phonons) and τ_I is the time interval between collisions with impurities. The probability of the scattering event can be described as a linear combination of probability of scattering by independent origins and thus

$$\frac{1}{\tau} = \frac{1}{\tau_L} + \frac{1}{\tau_I}$$

It is believed that for the graphene-based materials the impurity and defect scattering are the main sources for the reduction of scattering time. Oxygen

impurities arise from the oxidation process to widen the interlayer gap of graphite. Even after the graphene oxide film is formed after exfoliation, 20-50% of oxygen groups exist. These oxygen groups destroy the sp^2 network of graphene, making graphene a non-conductor, and thus must be removed through an appropriate reduction method.

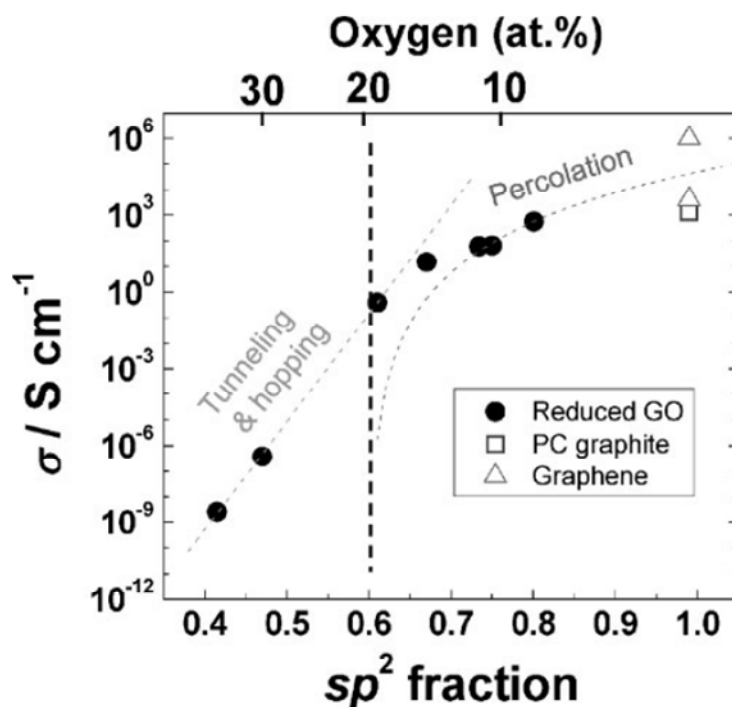


Figure 1.4.2 Electrical conductivity of thermally reduced GO as a function of the sp^2 carbon fraction ³⁸

As the oxygen content decreases by thermal or chemical reduction, the size of the sp^2 domain increases, which result in exponential enhancement of the electrical conductivity (Figure 1.4.2). Nevertheless, the electrical conductivity achieved by simple elimination of oxygen groups is limited to

be below 10^5 S/m because many remaining structural defects originated from harsh oxidation and reduction processes. Many efforts are done by different methods to improve these impurities and defects, like chemical and thermal reductions, mechanical pressing, etc. as will be discussed in detail in following section.

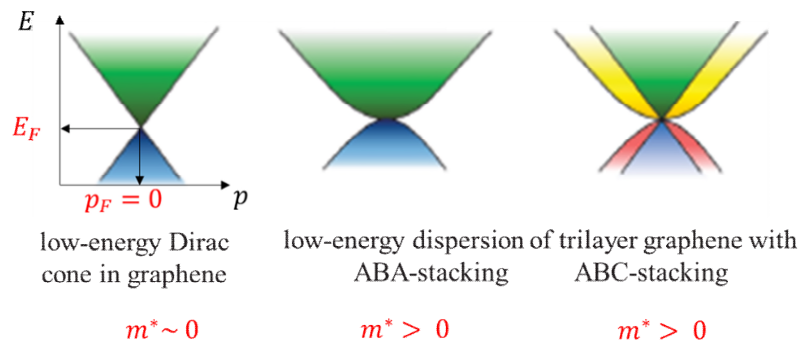


Figure 1.4.3 band structure of multilayer graphene depending on the stacking order

In addition to scattering due to defect and impurity, the stacking order of rGO film also may influence the electrical properties of rGO film. The linear band diagram of the monolayer graphene shows a massless behavior of the carrier quasi-particles inside the graphene, which plays a very decisive role in increasing mobility. However, the electronic structure of graphene-based materials is greatly influenced by the relative orientation between each graphene layer.³⁹⁻⁴² For example, it is known theoretically and experimentally that multilayer graphene with AB-stacking (or ABA-stacking) or ABC-stacking structure has a parabolic band diagram unlike graphene with linear dispersion (Figure 1.4.3). More interestingly, when graphene has a random stacking order (turbostratic stacking order), decoupling between each layer occurs even though it is multilayer graphene. There have been recent studies

that show that it can be significantly higher than AB-stacking graphite.³⁹⁻⁴²

1.5 Previous efforts to improve electrical conductivity of rGO free-standing film

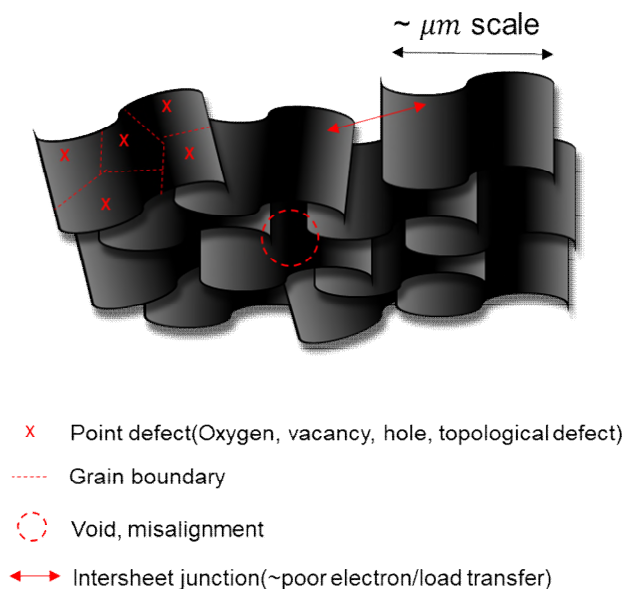


Figure 1.5.1 Structural defects limiting the electrical properties of rGO film

Pristine graphene, a material possessing the highest conductivity among existing material at room temperature, has low carrier density but extremely high mobility.^{2,43} The extremely high mobility of graphene is originated from its unique linear band structure resulting in the massless behavior of electrons traveling through the plane and low electron-phonon scattering at room temperature. In recent decades, the preparation of highly conductive macroscopic materials from graphene precursors has received great attention.⁴⁴⁻⁴⁶ However, the achieved electrical conductivity of reduced graphene oxide

(rGO) free-standing film²⁸ so far (10^6 S/m) is lower in orders than that of ideal graphene⁴⁷, conventional metallic conductors, and even comparable with commercial pyrolytic graphite sheets. The drop in electrical conductivity and mobility of rGO film is usually explained as being mostly due to a combination of scatterings at discontinuity including residual charged impurities⁴⁸, point defect⁴⁹, grain boundary⁵⁰, inter-sheet junctions^{51,52}, and misalignment²⁶.

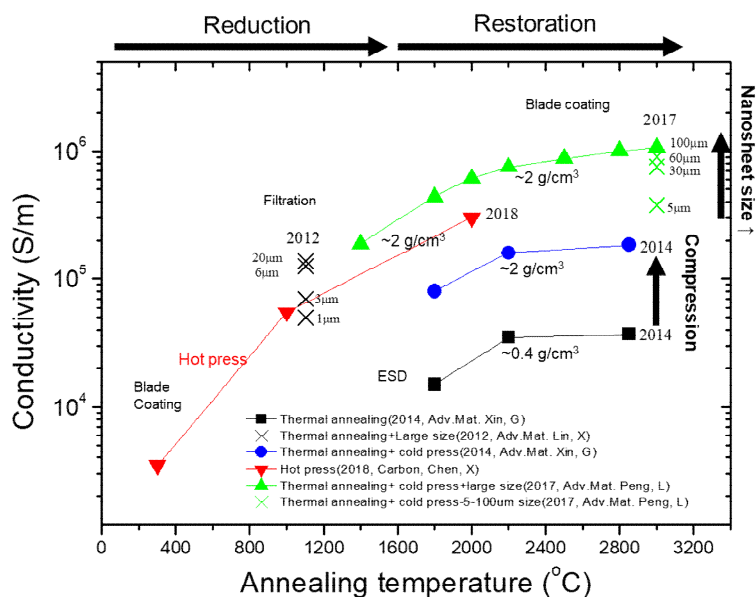


Figure 1.5.2 Previous works on improving the electrical conductivity of rGO film

Generally, the in-plane crystallinity of rGO film was found to be improved gradually by annealing at elevated temperature principally due to the decomposition of oxygen groups and recovery of sp^2 hybridized structure by bond rotation and vacancy migration.^{26,28} Thus, ultrahigh temperature graphitization of GO film is most successful and widely accepted for

researches shooting the highest electrical conductivity for EMI shielding or high-power electronics applications^{28,53}.

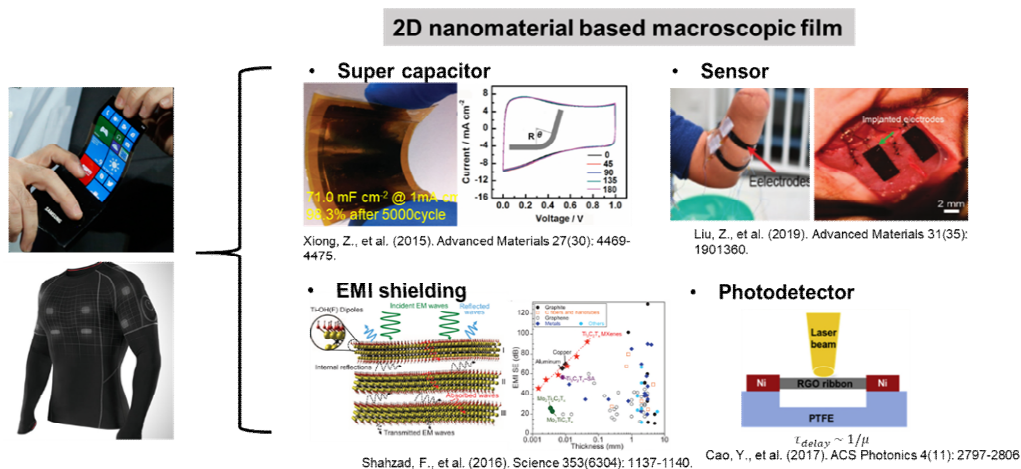


Figure 1.5.3 Applications of highly electrically conductive, flexible free-standing film

In addition to the restoration of in-plane crystallinity, the hierarchical structure of the rGO film must be optimized to achieve maximum performance of rGO film. For instance, non-parallel alignment or intersheet junction cannot be fully solved simply by high-temperature heating⁵³, so additional methods such as the optimization of assembly process^{35,54}, use of large-sized GO^{28,52,55-58}, mechanical compression^{26,59,60} are applied together with high-temperature annealing. On the other hand, bioinspired sheet to sheet cross-linking by polymer additives has been reported to enable highly efficient electron/load transfer between graphene interlayers.^{34,61-64} For instance, the great improvement of mechanical strength (~ 1 GPa) and a moderate improvement of electric conductivity were achieved by long-chain $\pi - \pi$ bridging of low defect GO sheet.^{64,65} However, because these polymer additives commonly lack thermal/chemical stability, post-treatment of the

films is limited to mild chemical reduction, which limits their electrical conductivity to be below 10^5 S/m.^{64,65}

Another parameter that also has a big effect on mobility is the effective mass. Effective mass is a mathematical device that simplifies the band structure by modeling the transport of electrons interacting with the lattice as free-particles having the corresponding mass. The effective mass is the measure of parabolicity of the band structure of semiconductors. It is well known that the graphene's unique properties (high electrical and thermal conductivity, high mobility, high mechanical strength, etc.) are due to its linear dispersion (zero effective mass near Dirac point) of the band structure near Fermi level and it is due to the 2D structure. This linear band-structure provides no band-gap at pristine graphene. There many theoretical and experimental efforts done for the understanding and control of band-structure of graphene to utilize it as a semiconductor with the high mobility at transistor technology.

Several recent studies revealed that the effective mass and Fermi-velocity in multilayer graphene can be significantly altered by engineering stacking order. The existence of differences in stacking order of graphene-based materials has been reported by Raman 2D band analysis, Transmission electron microscopy, and X-ray diffraction analysis. In Raman, decoupled phonon in neighbouring layers of turbostratic stacking graphite can be observed by the symmetric single peak while the coupled phonon in AB-stacking graphite results in assymmetric peak that can be deconvoluted into three different Lorentzian peak. On the other hand, random orientation of the layers are known to increase interlayer spacing up to the 0.34 \AA while the spacing of the AB-stacking graphite is around 0.33 \AA . Moire pattern in TEM image or ring pattern in electron diffraction also have been used to estimate the local

stacking order of graphite-like materials. Most interestingly the electronic structure of multilayer graphene are reported to be resemble monolayer graphene. The linear band structure of monolayer graphene can be retained even for the bi-layer graphene when it is turbostratically stacked while the AB-stacked multilayer graphene possess parabolic band diagram. This theoretical researches naturally brought the implication that the superhigh carrier mobility of pristine monolayer graphene originated from massless behavior of electrons possibly can be retained in the multilayer graphene with turbostratic stacking.

Indeed, recently the carrier mobility of turbostratic stacking multilayer graphene on SiO₂ substrate was measured to be much higher than that of AB-stacking multilayer graphene or even that of single-layer graphene.^{41,66 59,67}

Recently, several studies suggest that stacking order also has a significant effect on the macroscopic properties of the graphene free-standing film. By the way, the thermal conductivity⁶⁸ and mechanical strength⁵⁹ of the graphene film with mixed stacking order can exceed that of pyrolytic graphite. However, the effect of stacking order on the electrical properties of rGO film is rarely reported so far. In this sense, the bottleneck of the electrical conductivity can be naturally understandable since the ultrahigh-temperature annealing results in not only restoration of in-plane crystallinity but also the transformation of turbostratic stacking region into AB-stacking region.⁵³ Therefore, It is an important topic that determining the effect of stacking order on the carrier transport properties of the rGO film and engineering the stacking order of high temperature annealed rGO film.

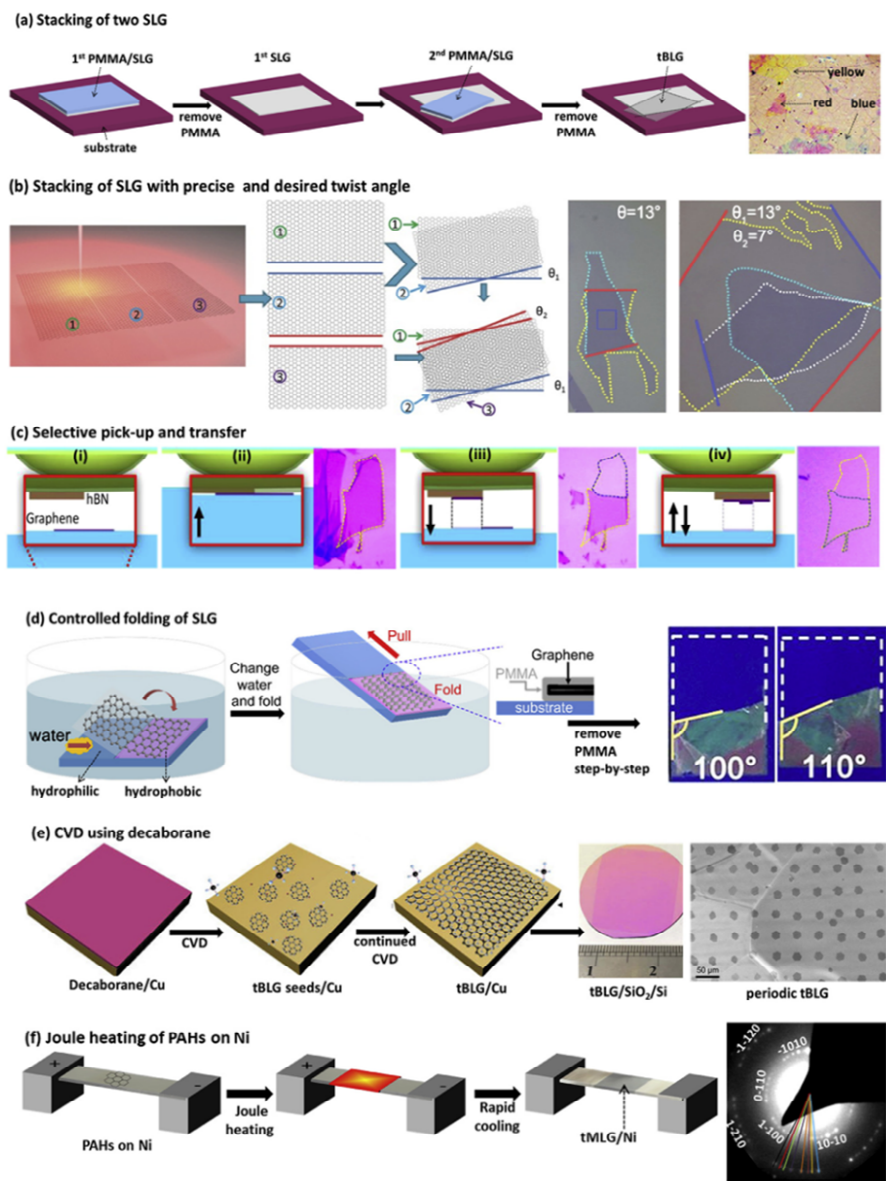


Figure 1.5.4 Previous efforts to synthesize the turbostratic stacking multilayer graphene⁴²

Previous efforts to make turbostratic stacking multilayer or macroscopic

graphene film are mainly based on two approaches: bottom-up and top-down. In bottom-up synthesis, the chemical vapor deposition (CVD) method is a representative method, the graphene layer easily rotates during growth and accumulates in AB-stacking, the lowest-energy stable structure.^{69,70} To deal with this fundamental limitation, a method of repeated transfer of large-area single-layer graphene⁵⁹, controlled folding⁷¹, and preventing the rotation of the graphene layer during growth in a vapor-solid growth process^{72,73} have been proposed. Although some of these approaches are possible to control the twisted angle, the limited scalability of the CVD method makes it unsuitable for making macroscopic turbostratically stacked graphene materials.

To compensate for scalability, an attempt has been made to synthesize turbostratic stacking graphene from pyrolysis of various precursors. The stacking order of pyrolyzed graphene-based material is highly dependent on the type and structure of precursors. For example, combustion of magnesium in a carbon dioxide environment or pyrolysis of infiltrated poly (catecholamines) in GO film is reported to generate graphene film with mixed stacking order. On the other hand, the hierarchical structure of GO film has also been reported to have a great influence on the transformation of turbostratic stacking into AB stacking during high-temperature heating. For example, Wang et al reduced the portion of turbostratic stacking by reducing the thickness of the precursor GO film and achieved a portion of ~37% even with 2850°C annealing.⁶⁸ However, a general understanding of the required structure of the precursor and mechanism of stacking order regulation in these top-down approaches has not yet been discussed clearly.

Recently, techniques have been developed to tailor the hierarchical structure of graphene oxide film by first forming GO into an ordered phase in colloidal

dispersion, for example, nematic-phase liquid crystalline solutions⁷⁴ or hydrogels^{34,61}. Generally, GO hydrogel can be obtained by adding a binder or by adjusting the solvent properties to strengthen the attractive force between GO sheets moderately.⁷⁵ Fragmentation-assisted gelation using sonication or laser was proposed as a method of forming a thermally and chemically stable graphene-based porous 3D structure without any additional additives.^{76,77} Besides various applications utilizing a high specific area of this porous structure, There have been attempts to control the structure and properties of GO and rGO films by using the cross-linked nature of GO hydrogel. For instance, Zhang et al reported that highly interlocked structure of cast-dried GO hydrogel greatly enhanced the mechanical strength of chemically reduced rGO film without sacrificing electrical conductivity^{34,61}.

Here, we demonstrated that the ultrahigh electrically conductive graphitization can be suppressed by limiting the relative motion of graphene flakes through sonication assisted gelation of GO precursor without any additives. Moderate annealing of binder-free GO hydrogel results in rGO film with highly restored in-plane crystallinity with retained turbostratic stacking. Electrical conductivity and mobility were maximized at the point where the interplay of stacking order and degree of the defects was optimized. It is demonstrated that the carrier mobility and conductivity of rGO film can be greatly improved with increasing turbostratic stacking order. The optimized film turns out to possess record-high mobility ($720 \text{ cm}^2 \text{ V}^{-1} \text{ s}^{-1}$) and record-high conductivity ($1.95 \times 10^6 \text{ S m}^{-1}$) exceeding commercial pyrolytic graphite sheet and even highly ordered pyrolytic graphite. This is a cost-effective green way to fabricate ultrahigh conductive graphene film for various potential applications such as EMI shielding and high-power electronics

Chapter 2

Aims and Motivations

2.1 Objectives and Scopes

Despite the continuing need for the highly electrically conductive carbon-based free-standing film for future flexible electronics, the electrical conductivity of the existing rGO free-standing film is limited to be below that of highly ordered pyrolytic graphite. This bottleneck arises from the trade-off between the removal of in-plane defects and the accompanying graphitization in the structural restoration process. In other words, thermal rearrangement of carbon in rGO film at high-temperature not only eliminates the oxygen and in-plane defects but also transform the turbostratic stacking region into the AB-stacking region, which limits the electronic band structure of rGO film to be parabolic even when in-plane crystallinity is highly restored.

In this study, the correlation between the structure and electrical properties of the reduced graphene oxide (rGO) free-standing film was experimentally investigated for the first time, and a facile synthesis method for the rGO film with record-high electrical conductivity and record-high carrier mobility was proposed.

2.2 Hypothesis

The effect of the stacking order of rGO films on the electrical properties has not been systematically reported yet. However, there were several previous studies conducted on the correlation between the electrical conductivity and the stacking order of multilayer graphene. However, based on the fact that the conductivity of the previous study remains at HOPG, we assume that if the in-plane crystallinity is recovered more than a certain degree, the stacking order will affect the effective mass and Fermi velocity of the rGO film and, in the end, will greatly influence the electrical conductivity.

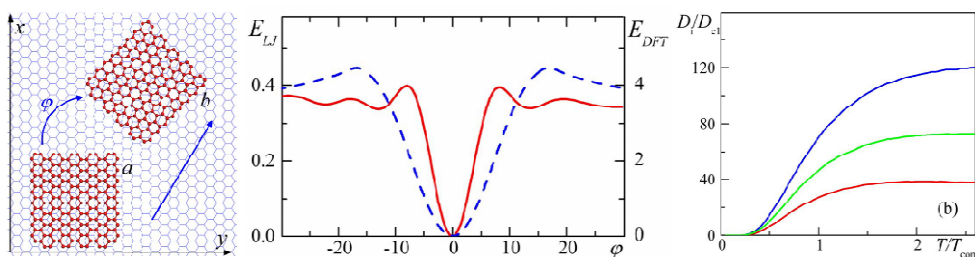


Figure 2.2.1 Rotational diffusion of a graphene flake on a graphene layer⁷⁸

In order to maintain the turbostratic stacking order as much as possible, we tried to minimize the graphitic portion of rGO instead of maximizing the recovery of in-plane crystallinity by fixing the annealing temperature below 1800°C, the temperature at which graphitization just started. Although the mechanism of the formation of the graphitic portion of the rGO film has not yet been clarified, flake rotation by high-temperature heating suggested in previous studies was taken as the possibility.⁷⁸ In these theoretical studies, it has been suggested that the energy barrier and frequency of spontaneous flake diffusion and rotation are affected significantly by the size of a flake (Figure

2.2.1).

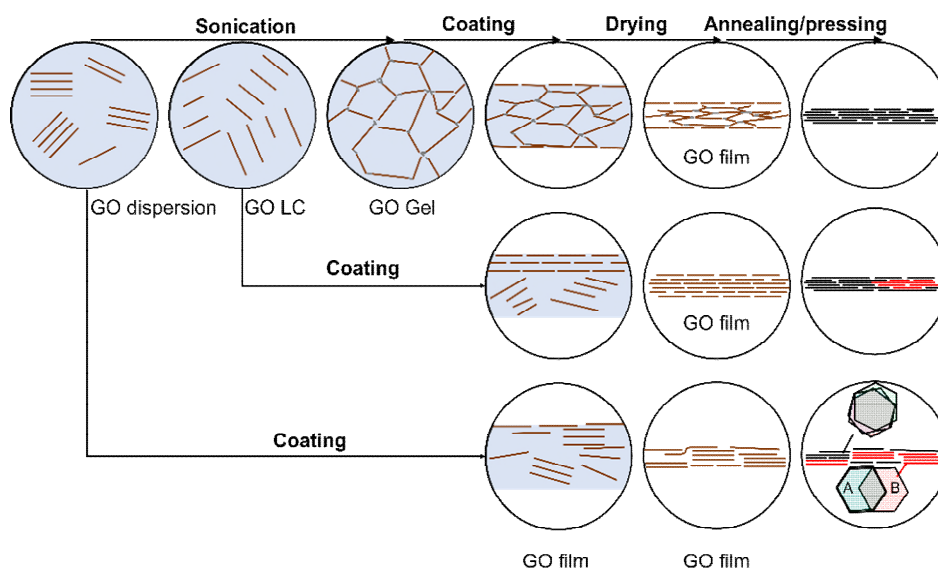


Figure 2.2.2 hypothesis on the regulation of stacking order by engineering GO precursor

Therefore, we tried to suppress the relative reorientation that occurs during high-temperature heating by inducing physical bonding between the nanosheets constituting the rGO film (Figure 2.2.2). Zhang et al synthesized a gel film by cast-drying polymer-induced and thermal annealing-induced GO hydrogel and studied its structure and strength improvement. Unlike solution-based films in which the Brownian motion of nanosheets is free, nanosheets of gel-based films have an interlocked structure due to their limited mobility. Unlike the solution-based film where small size sheets are mainly stacked on top by the Brownian motion of the nanosheets, both sides were symmetrical in the gel-based film, and this was confirmed by observing the cross-section with SEM during the drying process. It was confirmed that the film has such an interlocked structure that significantly improved the strength compared to

the film that did not.

In 2012, Owen, C. Compton, et al. reveal that GO hydrogel can be prepared by ultrasonication of GO dispersion without any additive. Pre-exfoliated aqueous graphene oxide dispersion with a concentration of 0.5mg/ml to 20mg/ml was further sonicated for a period of 120 min using a pulse probe sonicator. They observed that the viscosity increased with the sonication time and that the sheets were connected to each other by observing the card-house structure of the lyophilized sample. By observing the fragmentation of the sheets (~590nm to ~80nm) without chemical change (XPS, FTIR) during sonication they hypothesized that fracturing the nanosheets to generate smaller fragments that feature no carboxylic acid groups along their freshly exposed edges should decrease their dispersibility, but not induced irreversible aggregation. As for the type of bonding, it was said that mainly non-covalent bonding contributes to the gelation by observing that the gel breaks when diluted with water, but a more specific bonding type was not specified. They pointed out that these discoveries can be potentially adapted for the application of storage, delivery particularly concerning sensitive cargos.

To minimize additional impurities and gases generated during the heating process, we investigate the effect of gelation of GO precursor on the structure and electrical properties of rGO film by employing a sonication-assisted gelation method without the use of a binder. In short, we hypothesize that the highly connected nature of sonication-assisted GO hydrogel-based GO film can suppress the reorientation of graphene flakes forming AB-stacking region during high-temperature annealing.

Chapter 3

Method & Materials

3.1 GO Synthesis, GO hydrogel synthesis

Graphite oxide was synthesized from high purity graphite flakes (SP-1, Bay Carbon) using a modified Hummers method¹². Graphite (1.4 g) was stirred in 95wt % H₂SO₄ (70 mL). KMnO₄ (4.2 g) was gradually added to the solution while keeping the temperature <10 °C using a chiller bath. The mixture was then stirred at 35 °C for 3.5 hr. The resulting mixture was diluted by water (70 mL) under vigorous stirring and cooling so that the temperature did not exceed 50 °C. The suspension was further treated with 30 wt% aq. H₂O₂ (3.5 mL). The resulting suspension was purified by repeated centrifugation from water. The resulting graphite oxide was centrifuged for isolation and cast dried at 40°C for further use.

GO hydrogel was prepared via extended ultrasonication. GO cake was diluted to 16mg mL⁻¹, 10mL dispersion, and sonicated in an ultrasonic cleaner (POWER SONIC 610, 200W, HWASHIN TECH CO., LTD., Korea) for varying length of time. The resulting hydrogels were characterized by as-prepared. It should be noted that we used bath ultrasonication to obtain GO sheet rather than probe-type sonicator because it is known to be less invasive, allows easy control of sample temperature.⁷⁹

3.2 GO, rGO film synthesis

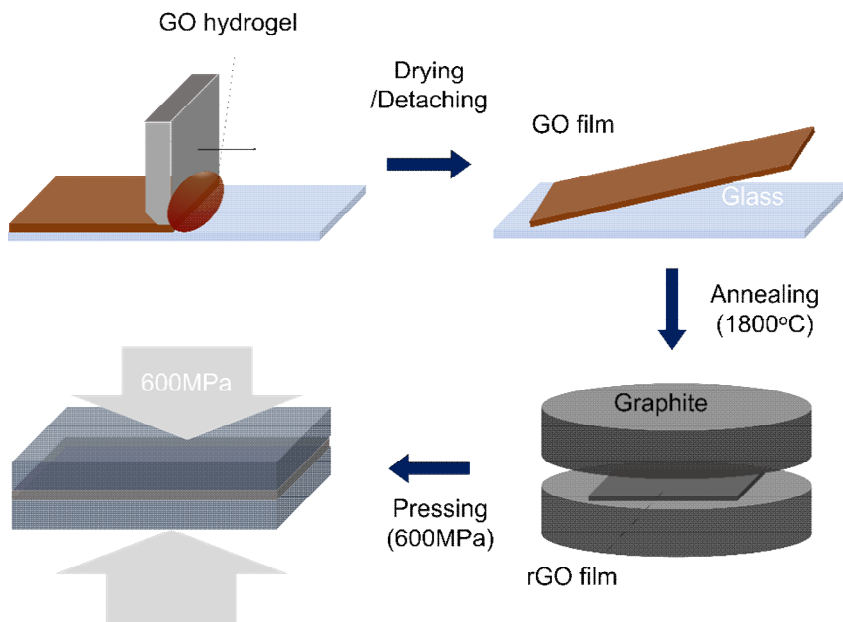


Figure 3.2.1 Fabrication process of free-standing graphene film from GO hydrogel

The methodology for highly conductive rGO film fabrication is based on a doctor blade coating of highly viscous GO hydrogel followed by high-temperature graphitization and mechanical compression as shown in figure 3.2.1.

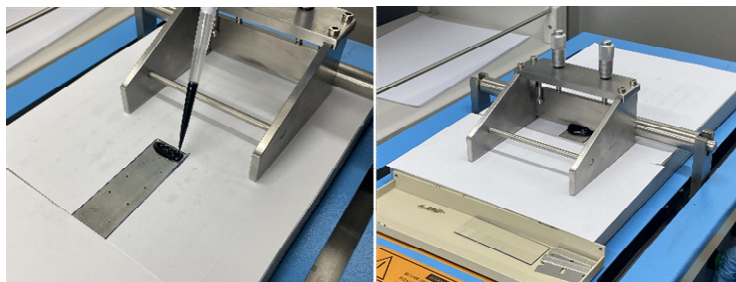


Figure 3.2.2 Digital photograph for GO hydrogel coating process

To achieve uniform freestanding GO film, the GO hydrogels sonicated were spread out on the prewashed glass substrate by an automatic blade coater (Figure 3.2.2). We controlled the hierarchical structure of the GO film precursor for rGO film by utilizing the structural evolution of GO hydrogel during the sonication. The wet GO films are dried overnight at 40°C and further dried in a vacuum oven to eliminate interstitial water as much as possible before the detaching process to minimize the interface cohesion force between GO film and glass substrate and expansion during the annealing process. The GO film could be detached by simply sliding a razor blade, resulting in the uniform GO film with a shiny surface (Figure 3.2.3).

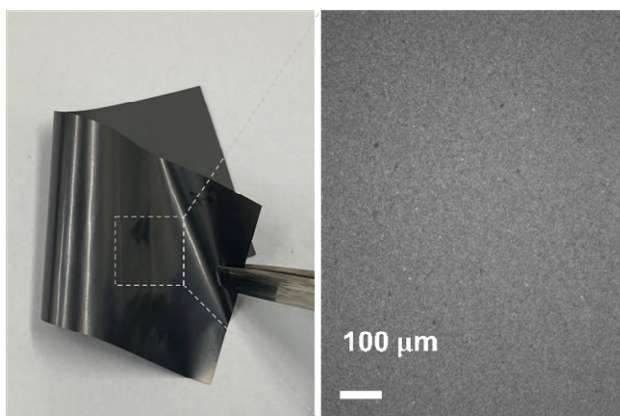


Figure 3.2.3 Digital photograph and optical microscope image for GO film after detachment

The mechanical properties of the resulting GO film are considerably high possibly because of the interlocking structure of GO hydrogel-based film (Figure 3.2.4).^{34,61} The value of tensile strength is around 780 MPa which is higher than that of 304 steel (505 MPa). Thanks to the strong nature of hydrogel-based GO film, GO film could be detached successfully without any noticeable damage on the surface.

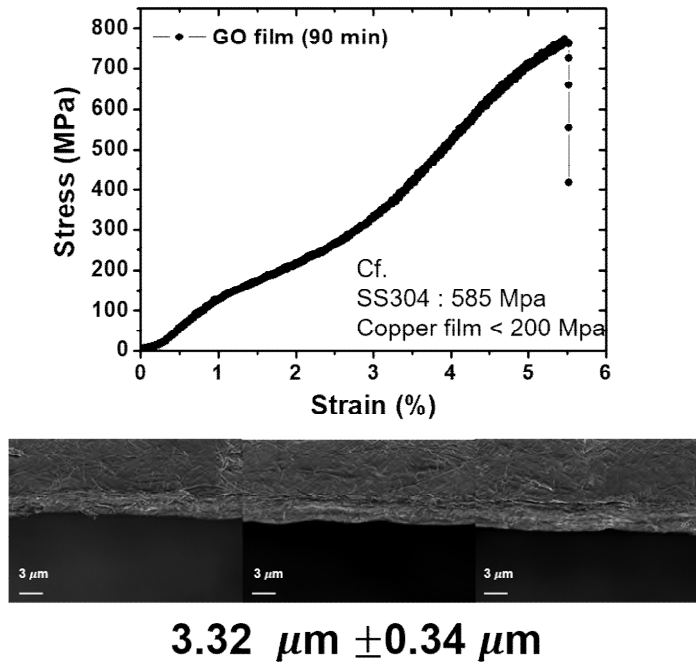


Figure 3.2.4 Stress-strain curve and cross-section of GO film

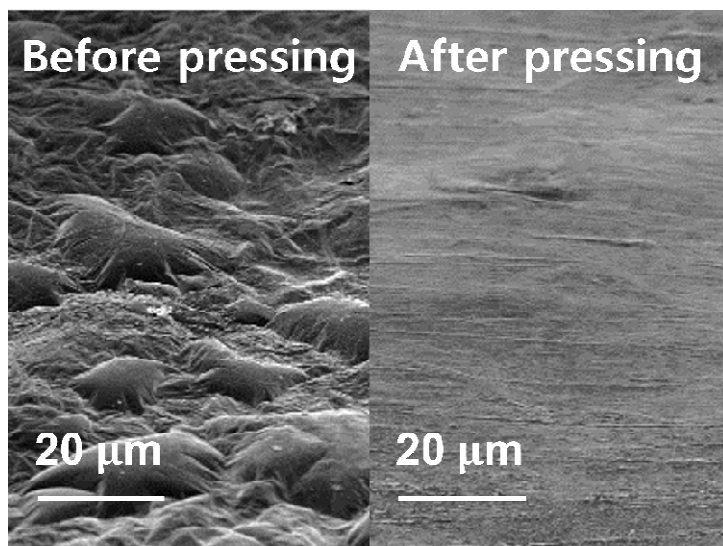


Figure 3.2.5 Top view surface of rGO film before and after mechanical pressing

After detaching successfully, the GO film was sandwiched by a pyrolytic graphite disc then annealed at 1800°C. Annealing condition is as follows. Heating rate: 20°C/min, dwell time at maximum temperature: 3hr, 10 min holding for every 200°C rise, 10-20°C/min cooling rate. Lots of air pores are generated inside the rGO film during thermal annealing as observed in figure 3.2.5. The air pores are likely originated from CO, CO₂, and H₂O gases evolution during thermal deoxygenation.⁸⁰ Following mechanical compression enhances the film alignment of the film and makes the thickness uniform by eliminating pores generated during the annealing process as shown in figure 3.2.5.

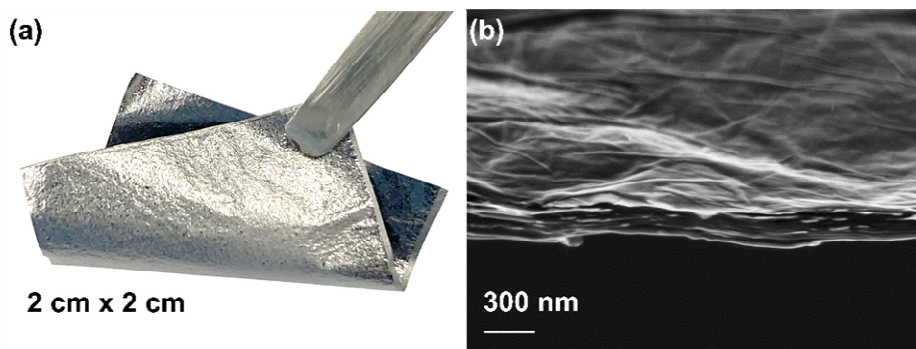


Figure 3.2.6 Digital photograph and cross-section SEM image of rGO film

The final rGO film shows shiny and uniform morphology with an average thickness of ~ 300 nm (Figure 3.2.6). Although there was $\sim \pm 10\%$ deviation from sample to sample in average thickness, the thickness of every sample was measured separately for estimating accurate electrical properties of the films. rGO films made from GO dispersions sonicated for different times and rGO films annealed at different temperatures were used for following structural characterization and electrical properties measurements.

3.3 Electrical conductivity measurements

Sheet resistance, often called sheet resistivity, is the extrinsic properties of thin films that are nominally uniform in thickness. Sheet resistance can be described by the resistivity, intrinsic properties of the materials as the following equation.

$$\rho = R_s t$$

A 4-point probe is commonly used to measure the sheet resistance of the film. Unlike the 2-point probe method, the 4-point probe has a great advantage in that it can offset the effect of contact resistance because the current source and voltage measurement are measured in separate electrodes. In particular, when electrical resistivity is very small (ie, contact resistance has a significant influence on the measurement), the sheet resistance of the film must be measured using a 4-point probe.

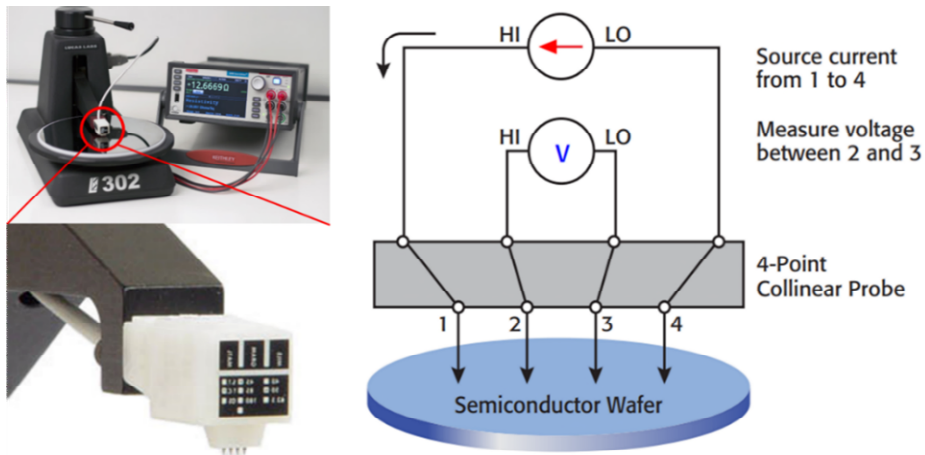


Figure 3.3.1 Typical 4-point probe equipment and schematic for operation principle

Pass current (I) between probes 1 and 4, and measure voltage (V) between 2 and 3. When the thickness of the sample is t, the resistivity is expressed as follows.

$$\rho = \frac{2\pi}{\ln 2} \frac{V}{I} t F \text{ (See below for demonstration)}$$

$$\text{or } \rho = R_s * t * F, \text{ where } R_s = \frac{2\pi}{\ln 2} \frac{V}{I}$$

In the 4-probe, the measured value is R_s (sheet resistance) in units of Ohm. To avoid confusion with resistance, it is expressed as Ω/\square or Ω/sq . F is a correction factor that considers edge effects and is determined by the ratio of the distance and thickness between the probes, the distance between the probes, and the width of the film. If the thickness is less than 0.5 times and the lateral size is more than 2 times larger than the distance between the probes, F can be approximated to 1. Since the distance between the probes in a typical 4-probe is in mm, it is approximated by $F=1$, and the resistivity can be measured only by knowing the thickness. The thickness is measured separately using SEM.

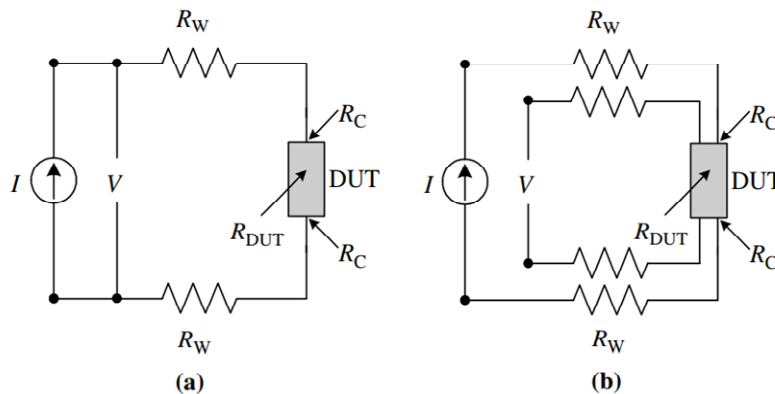


Figure 3.3.2 Two-terminal (a) and four-terminal (b) resistance measurement conceptual diagram

Considering the situation of the 2-point probe as shown in (a) in the figure above, the total resistance R_T appears as follows.

$$R_T = \frac{V}{I} = 2R_W + 2R_C + R_{DUT}$$

Where R_W is the resistance of the wire or probe, R_C is the contact resistance, and R_{DUT} is the resistance of the material to be measured. Since R_C and R_W are generally unknown and the only measurable parameters are V and I , it is of course not possible to determine R_{DUT} from the measured values using this method.

On the other hand, in the 4-point probe (b), the current path is the same as in (a), but the voltage is measured by adding two separate contacts and connecting a voltmeter between them. Of course, these two contacts also have the same contact resistance and wire resistance as in (a), but the current flowing into the voltmeter is very small due to the very high resistance of the voltmeter (more than 1012 ohms). Therefore, the voltage read by the voltmeter shows only the voltage drop caused by the current flowing through the DUT.

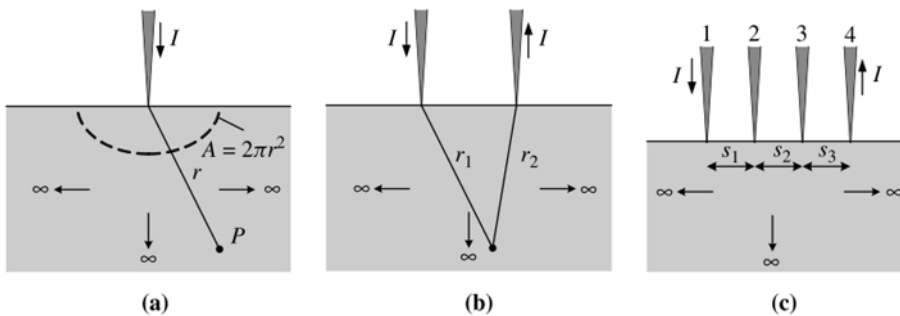


Figure 3.3.3 Current flow and voltage measurement of the 1-point probe (a), 2-point probe (b), and collinear 4-point probe (c)

Let's understand a simple structure like (a) in the figure above to derive the formula of the 4 point probe. The electric field E is related to the current density J, the resistivity ρ , and the applied voltage as

$$E = J\rho = -\frac{dV}{dr}, \quad J = \frac{I}{2\pi r^2}$$

Therefore, the potential of point P is as follows (when the potential of the probe is set to 0).

$$\int_0^V dV = -\frac{I\rho}{2\pi} \int_0^r \frac{dr}{r^2} \rightarrow V = \frac{I\rho}{2\pi r}$$

Therefore, in the case of (b), the potential at point P is as follows.

$$V = \frac{I\rho}{2\pi r_1} - \frac{I\rho}{2\pi r_2} = \frac{I\rho}{2\pi} \left(\frac{1}{r_1} - \frac{1}{r_2} \right)$$

Therefore, in case (c), the potentials at probes 2 and 3 are as follows.

$$V_2 = \frac{I\rho}{2\pi} \left(\frac{1}{s_1} - \frac{1}{s_2 + s_3} \right),$$

$$V_3 = \frac{I\rho}{2\pi} \left(\frac{1}{s_1 + s_2} - \frac{1}{s_3} \right)$$

Since the measured voltage value, $V = V_2 - V_3$

$$V = \frac{I\rho}{2\pi} \left(\frac{1}{s_1} - \frac{1}{s_2 + s_3} - \frac{1}{s_1 + s_2} + \frac{1}{s_3} \right)$$

In general, $s_1 = s_2 = s_3$, and in this case, if the above equation is summarized for resistivity ρ ,

$$\rho = 2\pi s \frac{V}{I}$$

For a typical 4-probe, the radius of the probe is 30-500um, and the spacing s between probes is 0.5-1.5mm. The smaller the probe spacing, the more accurate measurement is possible near the edge of the sample to be measured.

The above equation is the case when the sample is semi-infinite, and since there are edge effects, thickness effects, and lateral size effects by finite geometry, an additional correction factor F must be added.

$$\rho = 2\pi s \frac{V}{I} F$$

Correction factor

$$F = F_1 F_2 F_3$$

Where F_1 is thickness correction factor, F_2 is lateral sample dimension correction factor, F_3 is for placement of the probes relative to the sample edges.

If the thickness is t , and F_1 is F_{11} when the bottom of the sample is connected to a nonconductor, and F_{12} is when it is connected to a conductor,

$$F_{11} = \frac{t/s}{2 \ln\{\frac{\sinh(t/s)}{\sinh(t/2s)}\}}$$

$$F_{12} = \frac{t/s}{2 \ln\{\frac{\cosh(t/s)}{\cosh(t/2s)}\}}$$

(More detailed derivation is given in R.A. Weller, Rev. Sci. Instrument. 72, 3580–3586, Sept. 2001.)

In most measurement environments, measurement is performed on a non-

conductor, and since the thickness of the sample is much smaller than the distance between probes (in mm), it is $\sinh(t/s) \sim t/s$. In this case, it can be approximated by (see graph below).

$$F_{11} = \frac{t/s}{2 \ln(2)}$$

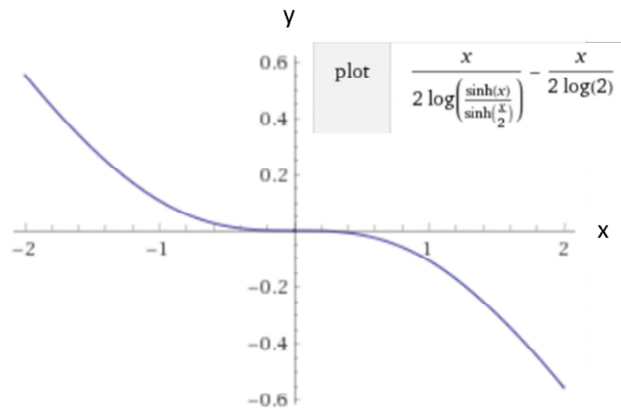


Figure 3.3.4 Approximation of thickness correction factor

Therefore, when the thickness of the film is less than half the distance between the probes, the resistivity of the film is as follows.

$$\rho = \frac{\pi}{\ln(2)} F_{xy} t \frac{V}{I} = 4.532 F_{xy} t \frac{V}{I}$$

where F_{xy} is size or shape correction factor

Since the thickness cannot be measured with a 4-point probe, $R_s = 4.532V/I$ is called sheet resistance, and the unit is set as Ω/square . The value measured by the 4-point probe is R_s , and to know the specific resistance and electrical conductivity, the thickness of the sample must be accurately measured

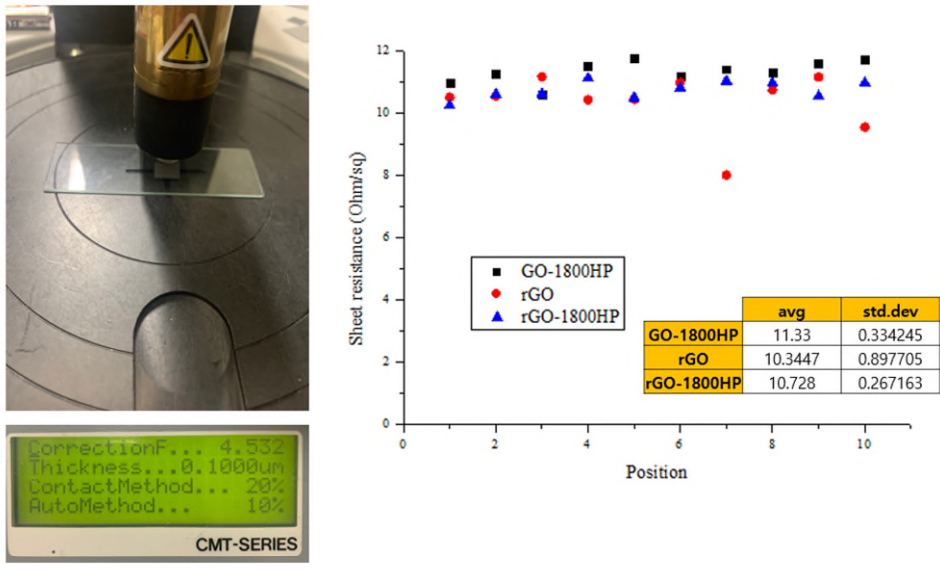


Figure 3.3.5 Repeated sheet resistance measurement by the 4-probe method

The 4-point probe used in this experiment is a device that automatically makes contact with the sample until a certain load or more is applied, and there is concern about damage to the sample due to the pointed probe tip. Accordingly, it was attempted to confirm the damaging effect by repeated measurement, and as shown in Figure 3.3.5, the increase in sheet resistance by repeated measurement was not confirmed.

3.4 Raman spectroscopy

Graphene's in-plane crystallinity is degraded by oxygen functionalities, point defects, and grain boundaries. The most widely used technique for measurements of in-plane crystallinity of carbon-based material is Raman spectroscopy. A schematic of a Raman spectroscopy is shown in the **figure**. In Raman spectroscopy, the sample is exposed under monochromatic light with a certain wavelength from a laser. By measuring the photon energy of scattered light from the sample, Raman spectroscopy can measure the phonon mode inside the carbon-based material. Most of the scattered light has the same energy as the excitation source, the process known as Rayleigh scattering. However, some optically excited electrons in the material emit light of lower or higher energy than that of the laser through the in-elastic scattering process(Stokes Raman scattering or Anti-Stokes Raman scattering respectively). Schematic for the working principle of typical Raman spectroscopy is given in figure 3.4.1.

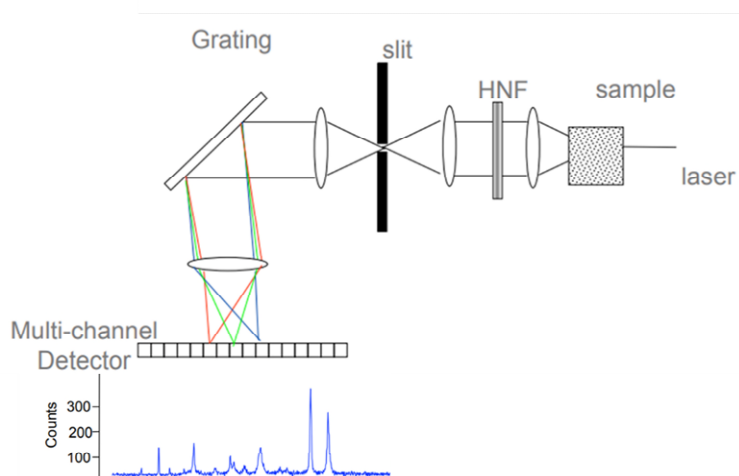


Figure 3.4.1 Working principle of Raman spectroscopy

Through measuring this energy difference, it is possible to investigate the phonon mode existing inside the carbon-based material. The D band that exists at $\sim 1350\text{ cm}^{-1}$ based on the 532nm laser is very sensitive to defects. If there is no defect, this mode is not coupled to the IR. However, as the discontinuity increases gradually, the coupling to the D band becomes possible, and by using this, the domain size or defect density can be inferred. On the other hand, the 2D peak, an overtone of D peak, is very sensitive to the three-dimensional ordering of graphene layers. For this reason, it is used to measure the number of layers of AB-stacked multilayer graphene, and it is also analyzed to observe the stacking order of graphitic materials. In the case of rGO film, when there are many AB-stacking regions, the 2D peaks show an asymmetric shape with peaks at 1680 cm^{-1} and 1720 cm^{-1} , respectively, whereas the turbostratic stacking rGO film has asymmetric 2D peak like monolayer graphene.



Figure 3.4.2 Raman spectroscopy equipment used in this study

In this context, we investigated the in-plane crystallinity and stacking order of rGO films prepared using Raman spectroscopy. Raman spectra were

obtained by the commercially available device (LabRam HR evolution, HORIBA Scientific, Japan) (Figure 3.6.2) at room temperature with 532 nm laser excitation. We choose the 532nm to ease the comparison with other researchers because it is the most common wavelength. The measured range was from 500 cm^{-1} to 3200 cm^{-1} to cover the D, G, and 2D bands. The equipment was first calibrated by a standard Si wafer with known resonance. ND filter was set to be 3.2% to avoid the damage of the sample by an intense laser beam. Hole and grating were set to be 200 and 600 respectively. Acquisition time was set to be the 60s while the acquiring number was set to be 2. Each phonon modes were analyzed by Lorentzian fitting. For instance, the 2D peak of the samples was deconvoluted into three different Lorentzian peaks centered at 2680 cm^{-1} , 2700 cm^{-1} , and 2720 cm^{-1} . The degree of defect inside our rGO film was estimated by calculation area ration between D and G band, which is represented as I_D/I_G . I_D/I_G can be converted into an in-plane domain size of rGO film by using Cancado's equation under the assumption that the structure of our high-temperature treated rGO film resembles that of polycrystalline graphite.

3.5 X-ray diffraction

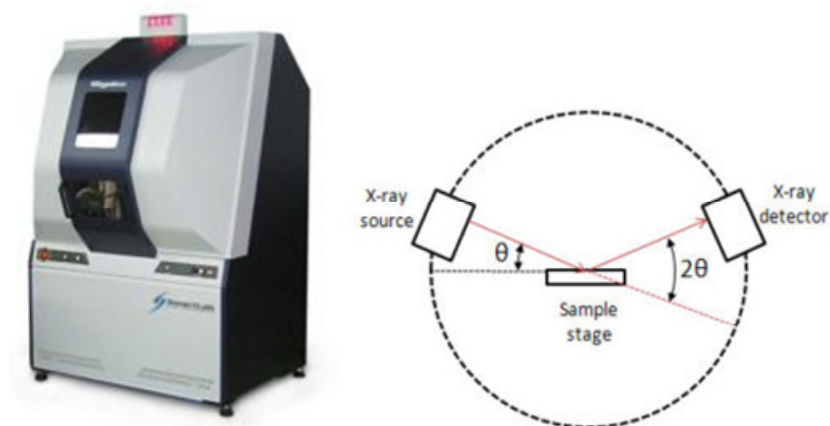


Figure 3.5.1 X-ray diffraction equipment used in this study

X-ray diffraction is the experimental technique determining the structure of a crystal. The periodic structure of crystalline material makes incident X-rays to be diffracted into specific angles. By measuring the angle and relative intensity of the diffracted beam, the type of crystal structure and the lattice constant can be calculated. The crystal is irradiated by monochromatic X-rays, producing a diffraction pattern of regularly spaced spots. When X-ray is irradiated into the species, spherical scattering takes place mainly because of atoms' electrons. A regular array of spherical waves are formed from a regular array of scatterers(atoms), which can make constructive interference in a few specific directions. The condition of constructive interference is described by Bragg's law.

$$2d\sin\theta = n\lambda$$

Where d is the neighboring distance between diffraction planes, θ is the

angle of incident, n is an integer, and λ is the wavelength of incident X-rays. We investigated the interlayer spacing of the 001 plane by irradiating X-ray diffraction on the rGO film. Two trends were investigated. Firstly, the reduction of the interlayer spacing by the removal of oxygen functional groups according to temperature.

3.6 X-ray photoelectron spectroscopy

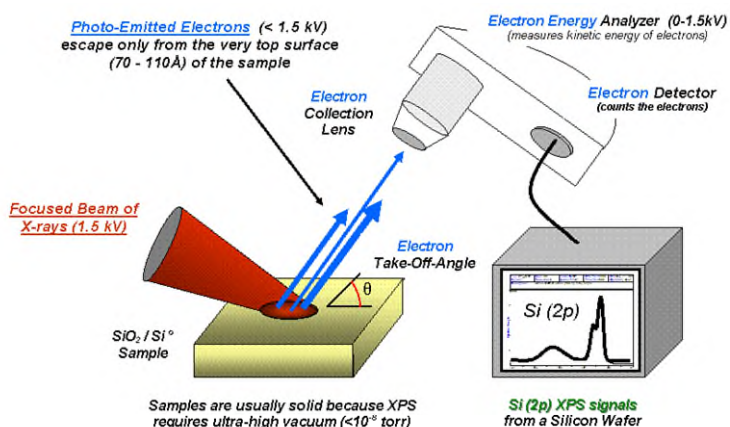


Figure 3.6.1 Working principle of X-ray photoelectron spectroscopy

X-ray photoelectron spectroscopy(XPS) is a spectroscopic technique based on the photoelectric effect, in which the energy difference between irradiated X-ray and emitted photoelectron is measured to find the binding energy of electrons within a material. XPS is a surface-sensitive quantitative measurement technique for the investigation of electronic structure. An elemental composition or chemical bonding inside the target materials could be obtained by analyzing the XPS spectrum because the electron's binding energy is highly dependent on not only the type of element but also its

bonding type with neighboring atoms. Soft X-ray is commonly used for XPS, which limits the measurement environment to be vacuum because of the strong absorption of soft X-ray in air.

In this study, XPS was used to measure the degree of reduction of rGO film according to temperature and the change of chemical composition of GO hydrogel according to sonication time. XPS spectra were obtained by the commercially available device(Axis Supra, Kratos, U.K). The Al $\kappa\alpha$ X-ray source was used and the vacuum was maintained below $5 * 10^{-10}$ torr. The ultimate energy resolution of the device is below 0.48 eV. The lateral resolution of the parallel imaging is $<1\mu\text{m}$. The chemical composition of the film was analyzed by calculating the area ratio of each element's peaks. For example, the C/O ratio is calculated by the area ratio between the C1s peak at around 285eV and the O1s peak at around 530eV. The bonding configuration was determined by deconvolution of each element peak.

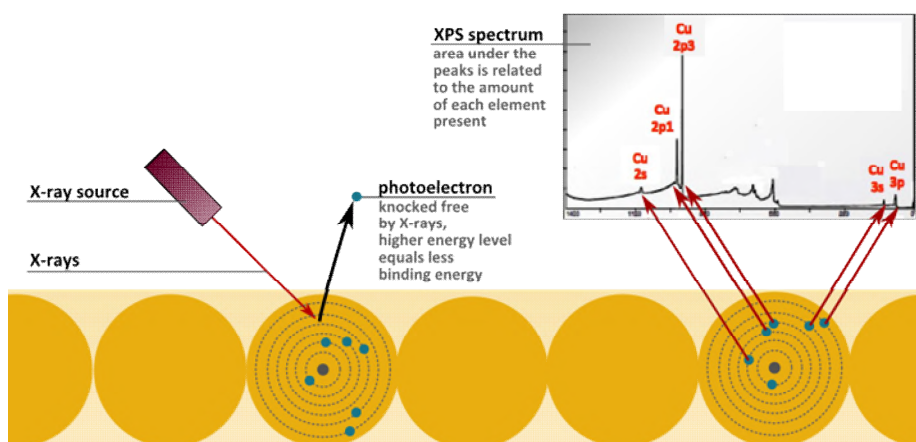


Figure 3.6.2 Principle of X-ray photoelectron spectroscopy

Chapter 4

Tailoring the electrical properties of rGO film by structural engineering

4.1 Various phase of GO dispersion

Colloidal systems in which interactions compete are known to exhibit a variety of dynamic stationary states because the system cannot reach a basic equilibrium state due to the limited motion of individual particles inside the dispersion. Graphene oxide is not only a precursor to obtaining chemically modified graphene but also possess many interesting properties in its own right. The unique balance between hydrophilic groups and hydrophobic graphitic domains inside the GO nanosheet make the GO possible to form various colloidal phase. GO has been shown to exhibit various arrested states of the aqueous dispersion phase such as glass, gel, and liquid crystals.

Recently, techniques have been developed to tailor the hierarchical structure of graphene oxide film by first forming GO into an ordered phase in colloidal dispersion, for example, nematic-phase liquid crystalline solutions⁷⁴ or hydrogels^{34,61}. Generally GO hydrogel can be obtained by adding a binder or by adjusting the solvent properties to strengthen the attractive force between GO sheets moderately.⁷⁵ Fragmentation-assisted gelation using sonication or

laser was proposed as a method of forming a thermally and chemically stable graphene-based porous 3D structure without any additional additives.^{76,77} Besides various applications utilizing a high specific area of this porous structure, There have been attempts to control the structure and properties of GO and rGO films by using the cross-linked nature of GO hydrogel. For instance, Zhang et al reported that highly interlocked structure of cast-dried GO hydrogel greatly enhanced the mechanical strength of chemically reduced rGO film without sacrificing electrical conductivity^{34,61}.

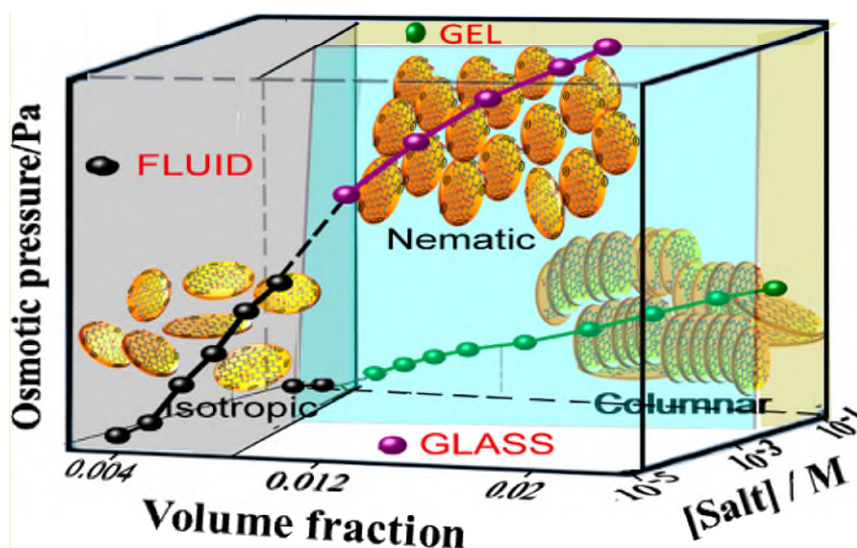


Figure 4.1.1 Various arrested states of GO dispersion⁸¹

4.2 Structural evolution of GO hydrogel during sonication

The chemical and structural evolution during sonication were investigated by various measurements for colloid sonicated for a different time. The microjet temporarily formed by the ultrasonic treatment spontaneously collapses and generates a strong shock wave, which transfers enough energy

to the exfoliate and fragment the graphite oxide that can be transformed into graphene oxide.

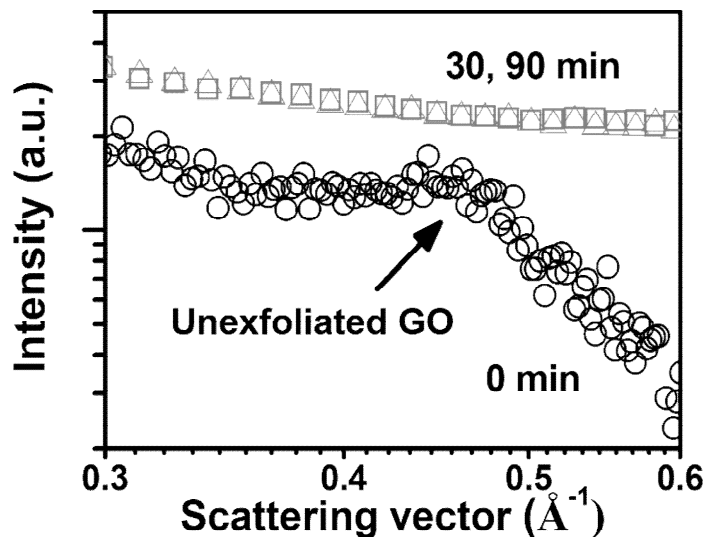


Figure 4.2.1 Degree of exfoliation with varying sonication time measured by WAXS

First, the exfoliation of graphite oxide by ultrasonic treatment was measured by wide-angle X-ray scattering (WAXS). It is confirmed that most of the particles are exfoliated by the disappearance of Bragg peak at $q = 0.45 \text{ \AA}^{-1}$ which corresponds to 1.4 nm interlayer distance. (Figure 4.2.1) This interlayer distance is consistent with that of unexfoliated graphite oxide in a water environment⁸²⁻⁸⁴.

As will be discussed in section 4.4, the unexfoliated graphite oxide is one of the possible origins of the graphitic stacking (AB stacking) region in the final rGO film because the graphite oxide itself is reported to possess AB-stacking even after reduction.⁸⁵ Thus, the high graphitic portion of rGO film made

from GO dispersion with short sonication time (< 30 min) may be partially due to the not fully exfoliated nature of the dispersion. In fact, as a result of conducting selected area electron diffraction measurement using a transmission electron microscope, it was confirmed that in the case of GO film made of GO hydrogel with sonication of <30 min, there is a non-negligible portion of AB stacking region even before thermal treatment (See section 4.4).

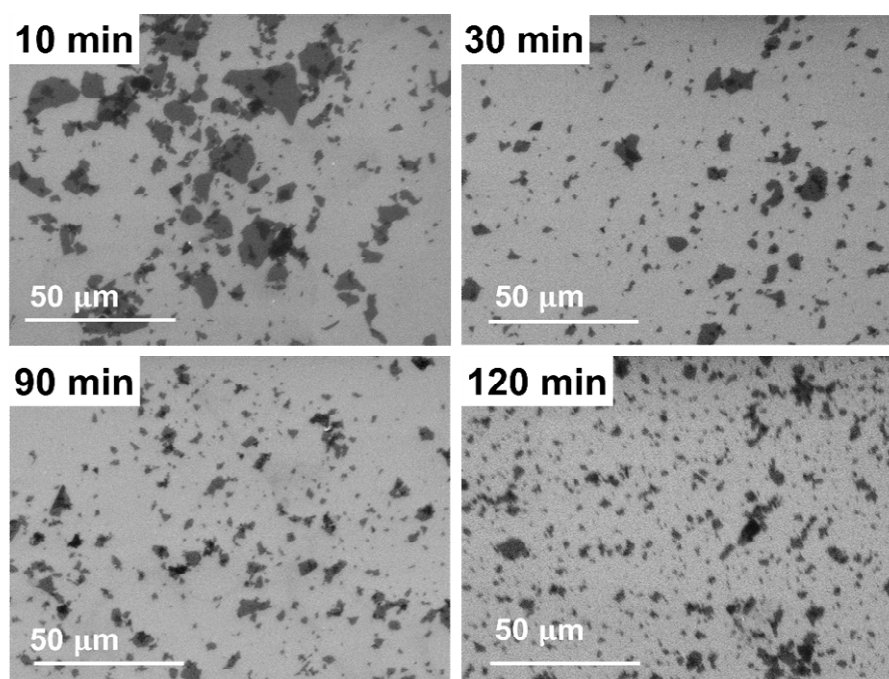


Figure 4.2.2 SEM images of drop cast graphene oxide nanosheets on SiO₂ wafer with different sonication time

Besides the sonication-induced exfoliation, sonication-induced fragmentation⁸⁶ and gelation⁷⁶ were investigated by measuring the sheet size of GO nanosheet and viscosity of the colloid. The average size of GO nanosheets is measured by SEM. Diluted GO dispersion is drop-casted onto

oxygen plasma-treated SiO₂ wafer. As expected, the sheet size is decreasing continuously with increasing sonication time (Figure 4.2.2).

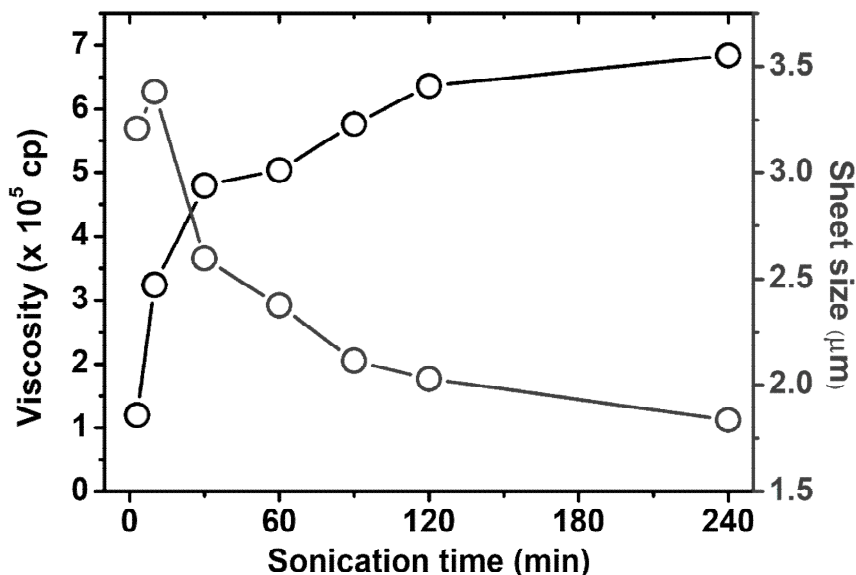


Figure 4.2.3 Viscosity and sheet size depending on the sonication time

Along with the fragmentation of the nanosheets, the rheological behavior of the resulting hydrogels varies greatly as a function of the time of ultrasonic treatment. When the ultrasonic treatment was started, a rapid increase in viscosity was observed in the first 30 minutes due to an increase in particle concentration due to the aforementioned exfoliation (Figure 4.2.3). The origin of the increase in viscosity continued after 30 minutes was supported by observing the structure of the lyophilized GO gel and the liquid crystallinity of the GO gel. Comparing to 30 min sonicated GO dispersion, lyophilized 90 min-treated GO hydrogel shows a more porous, card-house structure, which is a common characteristic in the cross-linked hydrogel system (Figure 4.2.4).

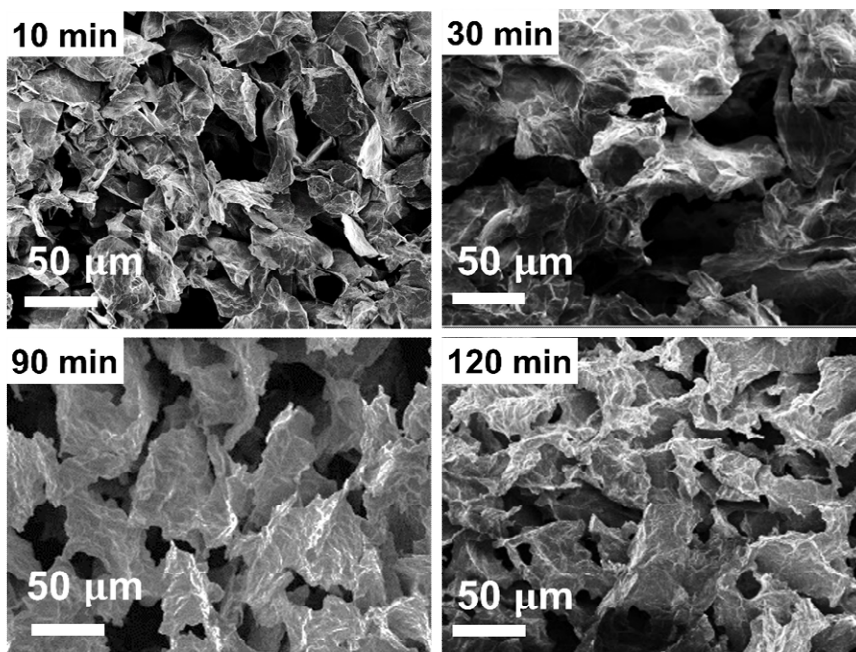


Figure 4.2.4 SEM images lyophilized hydrogels sonicated for the different time

This was also supported by the evolution of the SAXS 2D pattern. As the large graphite oxide particles are exfoliated and dispersed into graphene oxide, the particle density of the aqueous solution increases significantly. Graphene oxide has a property of repelling each other because it has a negative net charge by protonation of the carboxyl group and the hydroxyl group at the edge. According to Onsager's theory, when the concentration of the repulsively interacting discotic colloid becomes higher than a certain level, the particles tend to align in one direction to minimize entropy. This colloidal phase is called a liquid crystal and could be measured by SAXS 2D pattern or birefringence. However, extended ultrasonic treatment destroy this alignment confirmed by the isotropic circle SAXS pattern. (Figure 4.2.5)

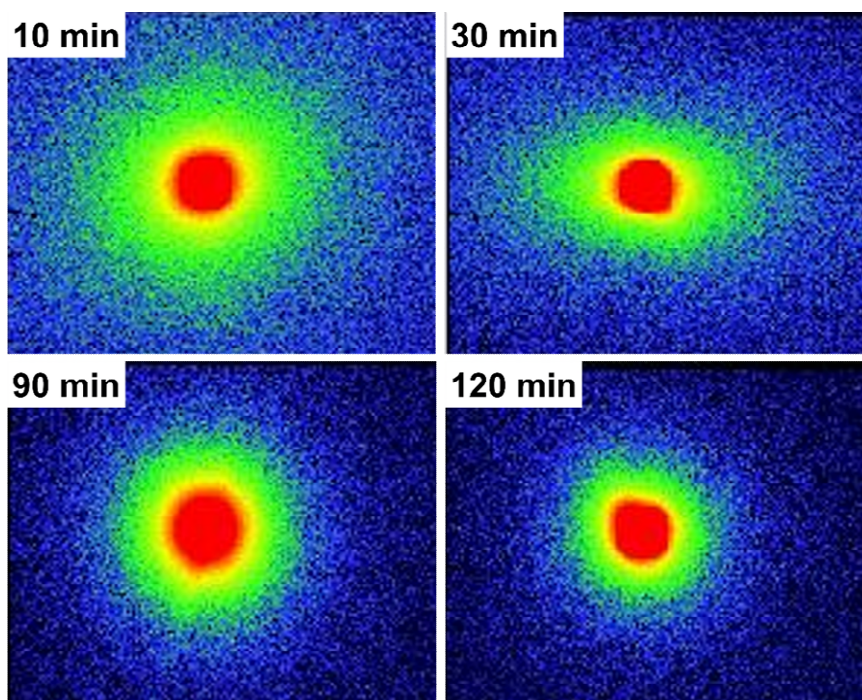


Figure 4.2.5 SAXS 2D pattern of the GO hydrogel sonicated for a different time

Summarizing the above measurement results, our GO dispersion experiences rapid exfoliation and continued fragmentation at the beginning, and accordingly, gelation proceeds to connect GO nanosheets. This is consistent with the several previous studies that suggest fracture-induced gelation.^{76,77} The freshly cleaved edge of fragmented graphene oxide nanosheet is a possible cross-linking site because the edge functionalization by oxygen groups such as carboxyl or hydroxyl group is the origin of the stability of graphene oxide aqueous dispersion.^{87 88 15} We postulate the phenomena will take place during the sonication treatment in this study because the concentration of the GO dispersion in this study is far beyond the critical gelation concentration suggested in these previous reports.

For sonication times of more than 30 minutes, all GO films before heating have a turbostratic stacking order consistent with much previous research. Nevertheless, the ratio of the graphitic portion after heating showed a large change from 25% to 10% depending on the viscosity of the GO hydrogel. It means graphitization behavior is significantly altered by the structural engineering of GO film. We hypothesized the interlocked structure of GO hydrogel is likely to limit the relative movement of graphene flakes during high-temperature heating. Unlike GO dispersion in which GO sheets are aligned by Brownian motion during the drying process of GO film, the mobility of GO nanosheets inside GO hydrogel is greatly limited, so the structure of GO hydrogel film is highly interlocked. This interlocking is thought to eventually limit spontaneous flake rotation during high-temperature heating.

4.3 Thermal deoxygenation and restoration of rGO film

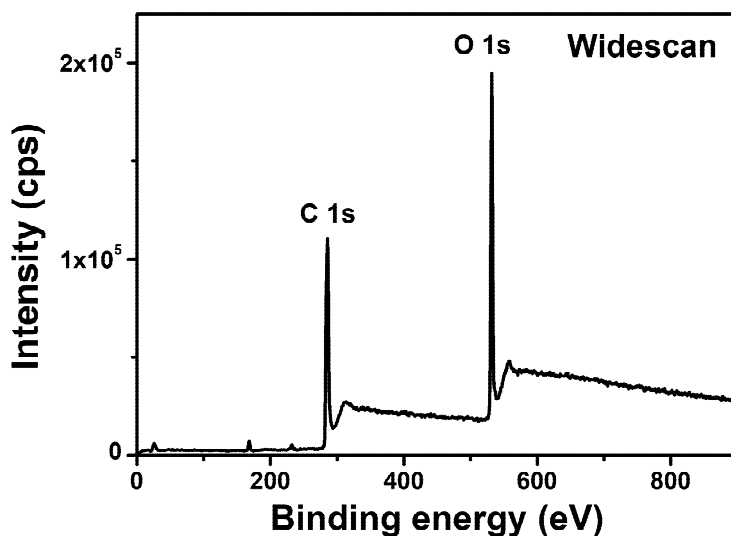


Figure 4.3.1 XPS spectra of graphene oxide film

The graphene oxide film before the reduction is decorated a lot with various kinds of oxygen groups. The type and amount of oxygen groups could be measured quantitatively by X-ray photoelectron spectroscopy (XPS). Counts per second according to the kinetic energy of collected electrons is plotted as a function of binding energy for a more intuitive interpretation. Looking at the XPS wide scan spectrum of the GO film before heating, the C 1s and O 1s peaks appear most prominently at around ~ 285 eV and 532 eV respectively. (Figure 4.3.1) Through this, it can be confirmed that oxidation and cleaning have been successfully performed.

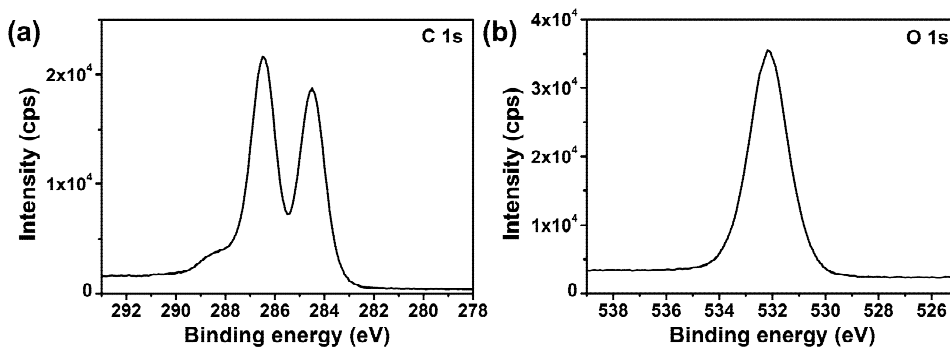


Figure 4.3.2 (a)C 1s and (b)O 1s peak in XPS spectra of the graphene oxide film

Quantitative elemental analysis using XPS requires the assessment of the intensities of the photoemission peaks of each element detected. For accurate analysis, correction of the background by electron inelastic scattering is essential, and we applied the Shirley background correction method. Looking at the C 1s peak with corrected background, it can be seen that in addition to the sp^2 hybridized carbon peak near 284.5 eV, a satellite peak of considerable intensity exists. (Figure 4.3.2 (a)) This satellite peak appears because the electron's binding energy changes as carbon binds to oxygen. This can be confirmed through the presence of a strong O 1s peak. (Figure 4.3.2 (b)) The C/O ratio can be calculated through the peak area ratio of C 1s and O 1s, and in the case of the above sample, the C/O ratio was about 2.44, which is mid-range among the various modified Hummer's methods.¹²

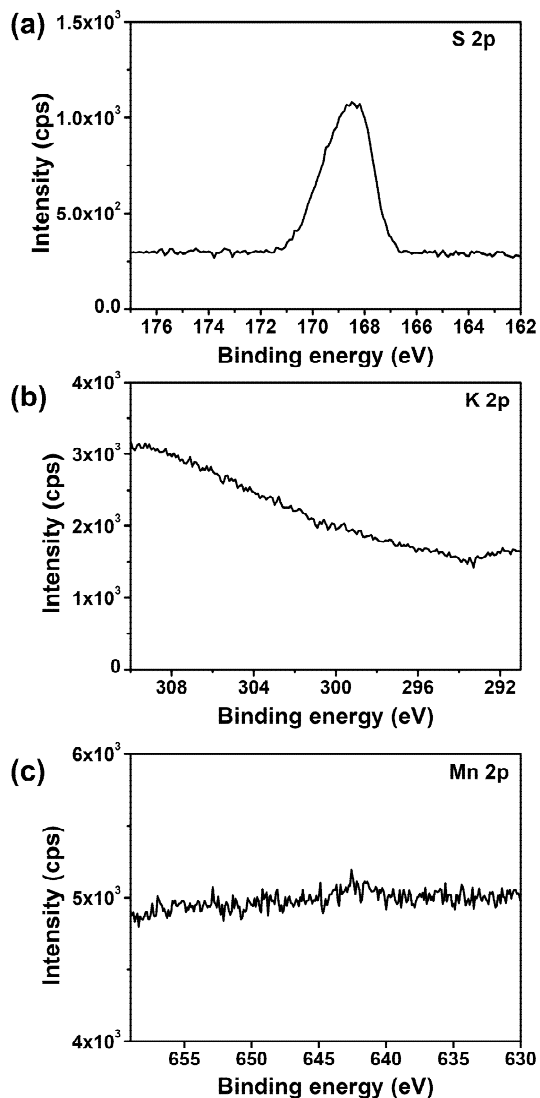


Figure 4.3.3 (a)S 2p, (b)K 2p, and (c)Mn 2p3 peaks

In the synthesis of graphene oxide, H_2SO_4 is used as a solvent, and KMnO_4 is used as an oxidizing agent. Although it went through the following cleaning process after oxidation reaction, the peaks for these elements were also measured and analyzed because residues of K, Mn, and S may exist. (Figure 4.3.3) As a result, it was observed that 0.95 at% of S and 0.1 at% of Mn were

present. Compared with other synthetic methods, this amount is quite small and we can confirm that our cleaning process was successful.

Table 4.3-1 Quantification of XPS analysis

	BE [eV]	FWHM [eV]	RSF	Atomic conc. [%]	Error [%]	Mass conc. [%]	Error [%]
S 2p	168.49	0.00	0.67	0.95	0.02	2.28	0.06
Mn 2p3	642.59	0.00	1.77	0.10	0.06	0.39	0.23
O 1s	532.19	0.00	0.78	28.78	0.13	34.38	0.16
C 1s	286.49	0.00	0.28	70.18	0.14	62.95	0.21

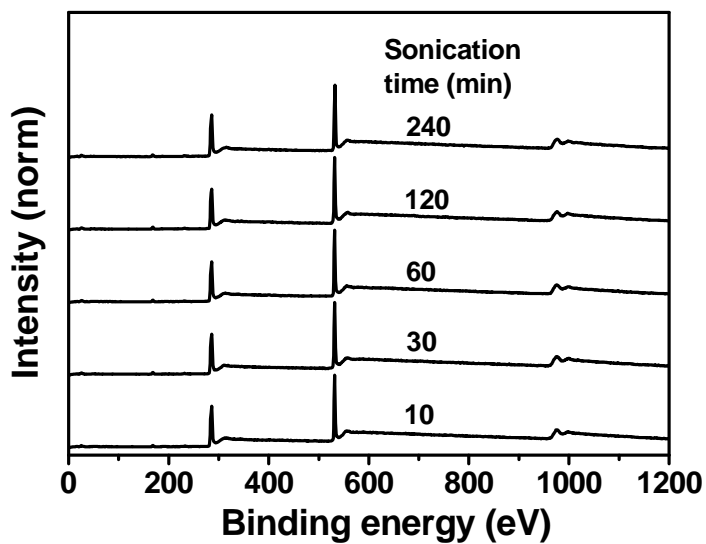


Figure 4.3.4 XPS wide scan with varying sonication time

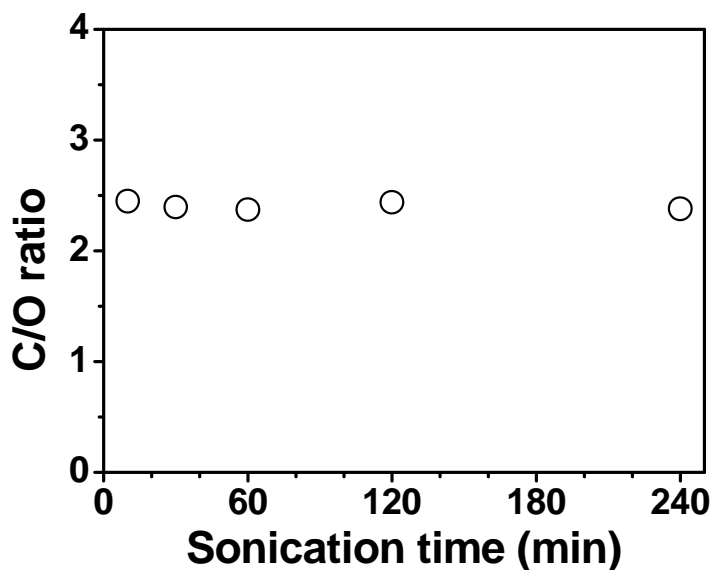


Figure 4.3.5 C/O ratio calculated from XPS analysis depending on the sonication time

Sonication induces fragmentation, and there is a possibility that freshly cleaved edges of GO nanosheets spontaneously oxidized. Therefore, we measured the chemical composition of GO hydrogel film according to sonication time using XPS and observed that oxygen contents hardly changed according to sonication time.[Figure 4.3.4 and Figure 4.3.5] It is inferred that the reason why the trend of change in oxygen contents was not observed despite fragmentation is that the freshly cleaved edge forms bonding between them rather than terminated with oxygen because fragmentation occurs under high concentration conditions.⁷⁶

To recover the conductivity of graphene oxide film, these oxygen groups should be eliminated by appropriate reduction techniques. In this study, to achieve the highest range of conductivity, high-temperature annealing is applied to fully eliminate the oxygen groups inside the graphene oxide film.

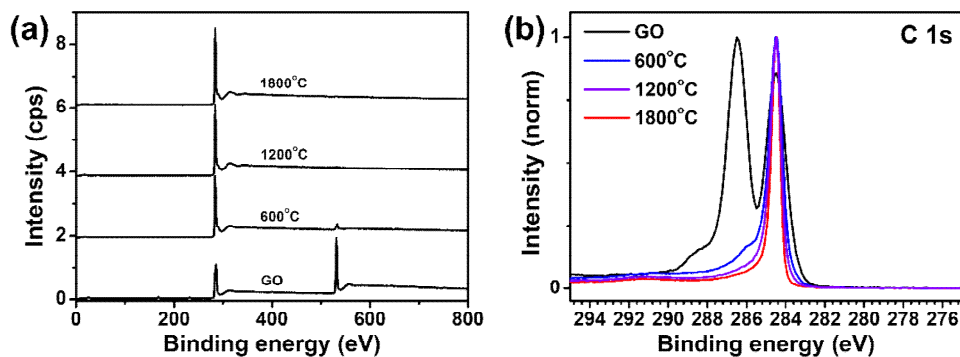


Figure 4.3.6 XPS wide scan spectra(a) and C1s peak (b)

The structure of the final reduced graphene oxide film is mainly determined by the chemical/structural characteristic of precursor and annealing temperature. First, the degree of gelation (120 min sonicated GO gel) is fixed to study the temperature effect. Oxygen contents that decrease with temperature can be measured through XPS analysis as above. As can be seen in Figure 4.3.6, the O1s peak, which was prominent in the GO state, tends to disappear after heating as the annealing temperature increases.

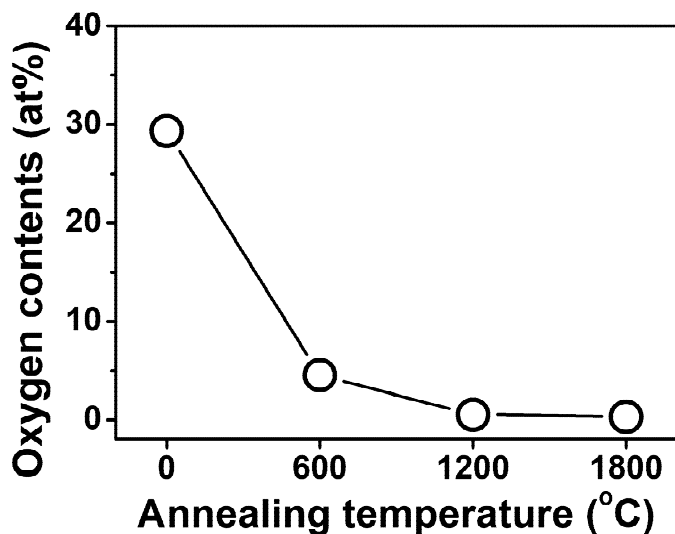


Figure 4.3.7 Oxygen contents of rGO film annealed at different temperature

Quantitative contents of oxygen inside the rGO film could be analyzed by estimation of area of O 1s peak. As expected, during the annealing process, the oxygen-containing groups are removed successfully. The oxygen content decreased from 29.37 at% to 4.49 at% (600 °C), 0.52% (1200 °C), and 0.28% (1800 °C) as shown in Figure 4.3.7. We should note that the oxygen content of 0.28 at% is quite small compared to other studies of rGO films heated at similar temperatures. This is possibly because there was no additional oxygen source due to binder-free synthesis, and the characteristic internal oxygen of the ultrathin film could easily escape. It was confirmed that the sulfur impurities before heating also completely disappeared after heating. [Figure 4.3.8]

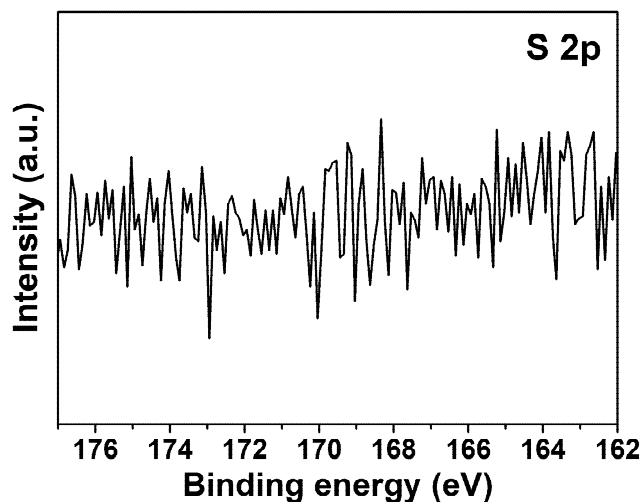


Figure 4.3.8 absence of S 2p peak in XPS spectra of 1800°C annealed rGO film

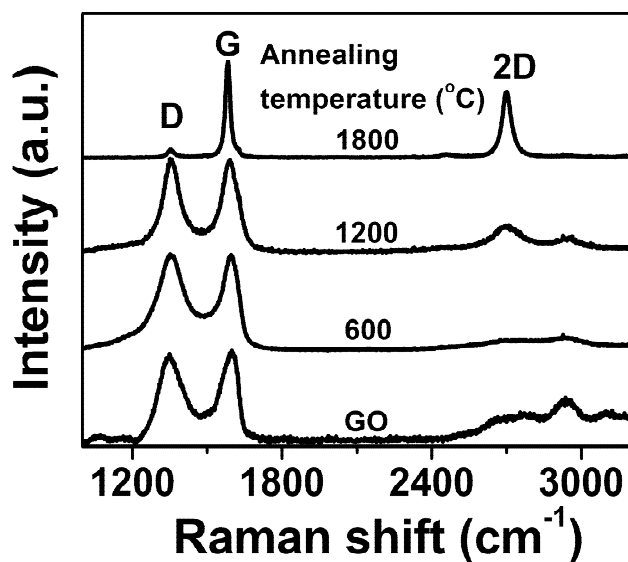


Figure 4.3.9 Raman spectra from GO and rGO film annealed at various temperatures

During high-temperature heating, oxygen is removed as well as active

rearranging of carbon lattice. In the high-temperature heating process, sufficient energy is given to cross the energy barrier that transforms the defective region into the semi-stable state before annealing into a hexagonal structure in the ground state. Therefore, as the heating temperature increases, vacancy defects and topological defects are healed, and the in-plane crystalline size gradually increases. This increase in in-plane domain size can be observed through Raman spectroscopy. In the Raman spectrum of carbon-based material, there are characteristic D peak and G peak, and D peak is excited by IR only when there is a discontinuity in the sp^2 network in graphene-based material. Accordingly, the degree of defect can be qualitatively measured by measuring the area ratio of D peak and G peak, and it can be quantitatively converted into domain size through the empirical formula proposed by Cancado et al.⁸⁹

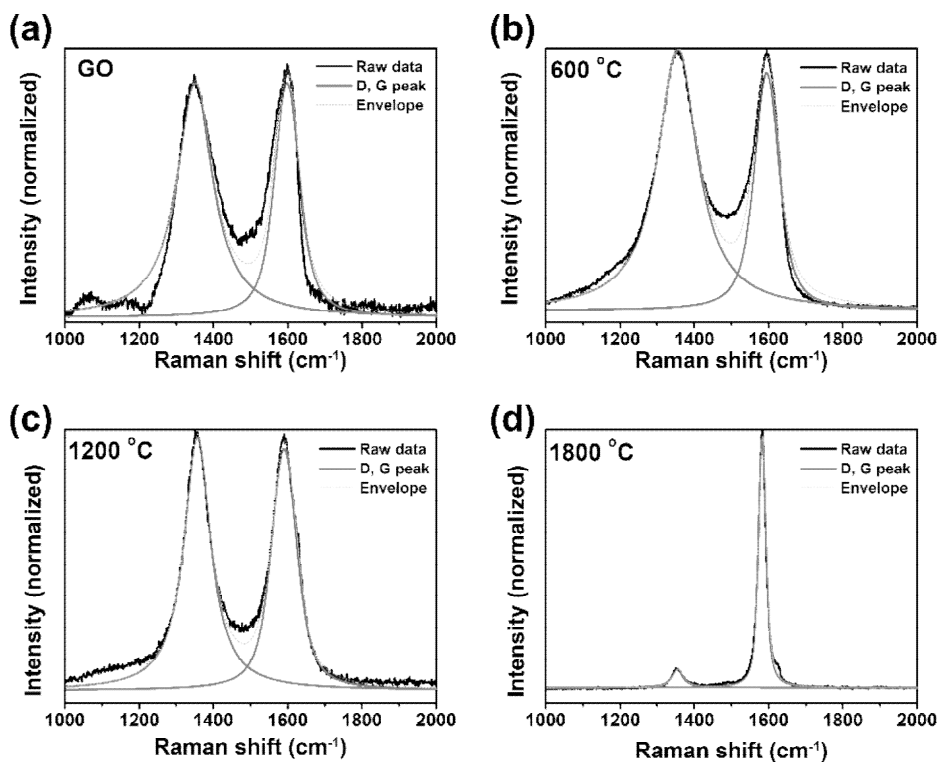


Figure 4.3.10 Deconvolution of D and G peak in Raman spectra of GO(a) and rGO film annealed at 600°C (b) 1200°C (c) and 1800°C (d)

To estimate the area ratio of G and D peak, the D peak was fitted with a Lorentzian function while the G peak was fitted with a Lorentzian function with a Gaussian distribution.⁹⁰ As can be seen in Figure 4.3.10, the D peak is located at $\sim 1350\text{ cm}^{-1}$ and the G peak is located between 1580 cm^{-1} and 1600 cm^{-1} . Depending on the annealing temperature, the intensity of the D peak decreases, and the FWHM of the G peak decreases. As a result, it can be concluded that defect healing is occurring according to the temperature. It can be seen that the relative area of the D peak increases with heating to 600 °C in GO, which possibly appears to be due to the overlapping of the area affected by the point defect.^{91,92} If the actual defect was increased, the FWHM

of the G peak should also be increased, but this trend was not observed. On the other hand, as oxygen was removed, carrier doping was reduced, so that the position of the G peak shifted from 1600 cm^{-1} to 1580 cm^{-1} . Most interestingly, there is a rapid decrease in D peak as the temperature increases from 1200 to $1800\text{ }^{\circ}\text{C}$, suggesting that active carbon rearrangement has occurred in this temperature range. Known graphene and graphite recrystallization starting temperatures vary from document to document, but are located around 1500°C which is consistent with our observation.^{53,89,93,94}

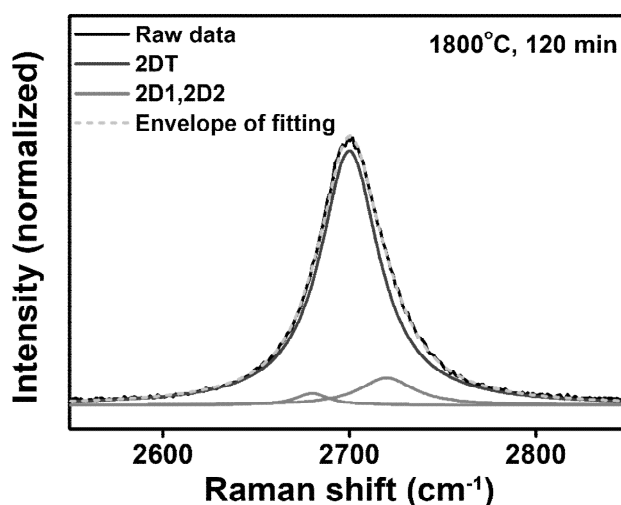


Figure 4.3.11 Deconvolution of Raman 2D peak

The stacking order of rGO film could be analyzed by the Lorentzian fitting of Raman 2D spectra.⁹⁵ 2D spectra of all samples could be deconvoluted into 3 Lorentzian peaks centered at $\sim 2700\text{ cm}^{-1}$ and $\sim 2680\text{ cm}^{-1}$, $\sim 2720\text{ cm}^{-1}$. The first peak at $\sim 2700\text{ cm}^{-1}$ is known to be originated from decoupled phonon in turbostratic stacking graphite while the other two peaks are originated from the AB-stacked graphitic region. According to Lorentzian fitting of the Raman 2D peak, 1800°C annealed rGO film is a mixture of turbostratic-

stacking and AB Bernal stacking domain.

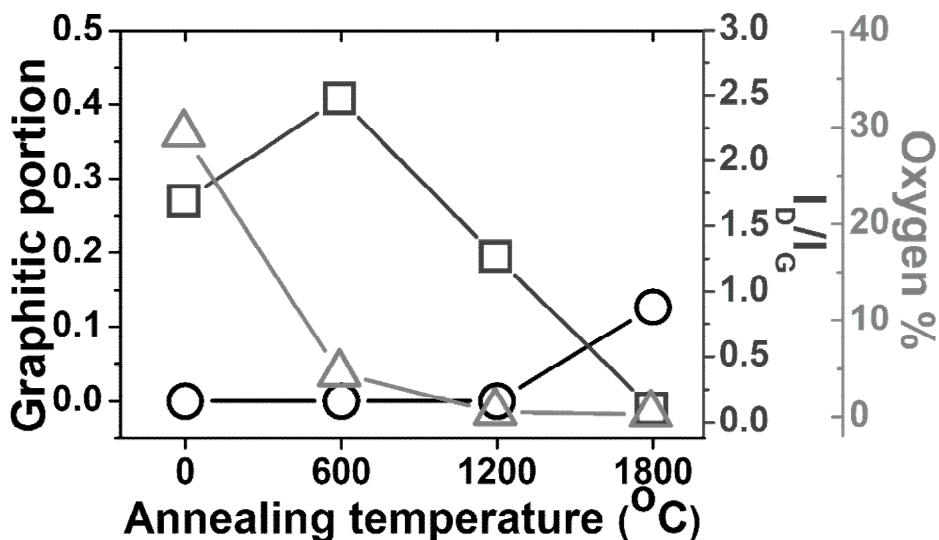


Figure 4.3.12 Graphitic portion, degree of defect, and oxygen percentage of rGO film depending on the annealing temperature

Along with the drastic restoration of in-plane crystallinity, the graphitic region, which did not appear at 1200°C heating, appeared at 1800°C to be ~10% of the whole film. Turbostratic stacking of rGO film is originated from the random overlapping of GO sheets during assembly, and a certain portion of turbostratic stacking is transformed into AB-stacking during high-temperature annealing possibly through the atomic vacancies immigration and spontaneous rotation of sheets.

4.4 Engineering of stacking order via precursor engineering

Along with temperature, the factor that greatly affects the structure and physical properties of rGO is the structural/chemical state of the GO film before heating. The structural/chemical state of the GO film can be controlled by changing or optimizing the fluid assembly method, or by changing the phase of the GO colloid. Recently, techniques have been developed to tailor the hierarchical structure of graphene oxide film by first forming GO into an ordered phase in colloidal dispersion, for example, nematic-phase liquid crystalline solutions⁷⁴ or hydrogels^{34,61}. Generally, GO hydrogel can be obtained by adding a binder or by adjusting the solvent properties to strengthen the attractive force between GO sheets moderately.⁷⁵ Fragmentation-assisted gelation using sonication or laser was proposed as a method of forming a thermally and chemically stable graphene-based porous 3D structure without any additional additives.^{76,77} Besides various applications utilizing a high specific area of this porous structure, There have been attempts to control the structure and properties of GO and rGO films by using the cross-linked nature of GO hydrogel. For instance, Zhang et al reported that highly interlocked structure of cast-dried GO hydrogel greatly enhanced the mechanical strength of chemically reduced rGO film without sacrificing electrical conductivity^{34,61}.

In 2012, Owen, C. Compton, et al. reveal that GO hydrogel can be prepared by ultrasonication of GO dispersion without any additive. Pre-exfoliated aqueous graphene oxide dispersion with a concentration of 0.5mg/ml to 20mg/ml was further sonicated for a period of 120 min using a pulse probe

sonicator. They observed that the viscosity increased with the sonication time and that the sheets were connected by observing the card-house structure of the lyophilized sample. By observing the fragmentation of the sheets (~590nm to ~80nm) without chemical change (XPS, FTIR) during sonication they hypothesized that fracturing the nanosheets to generate smaller fragments that feature no carboxylic acid groups along their freshly exposed edges should decrease their dispersibility, but not induced irreversible aggregation. As for the type of bonding, it was said that mainly non-covalent bonding contributes to the gelation by observing that the gel breaks when diluted with water, but a more specific bonding type was not specified. They pointed out that these discoveries can be potentially adapted for the application of storage, delivery particularly concerning sensitive cargos.

The electrical properties of graphene-based macroscopic films are greatly influenced by the stacking order in addition to in-plane crystallinity. Multilayer graphene stacked in AB-stacking order has a parabolic band structure like graphite, but multilayer graphene with turbostratic stacking order has been experimentally and theoretically proven that each layer can be decoupled to maintain a linear band. However, since high-temperature heating tends to transform the structure of the rGO film into a ground state, in addition to recovering in-plane crystallinity, there is a tendency to convert the stacking order to AB-stacking order. Therefore instead of removing the defect by raising the temperature further, we adjusted the hierarchical structure of the rGO film by inducing the structural change of the GO film by varying the sonication time of the GO hydrogel.

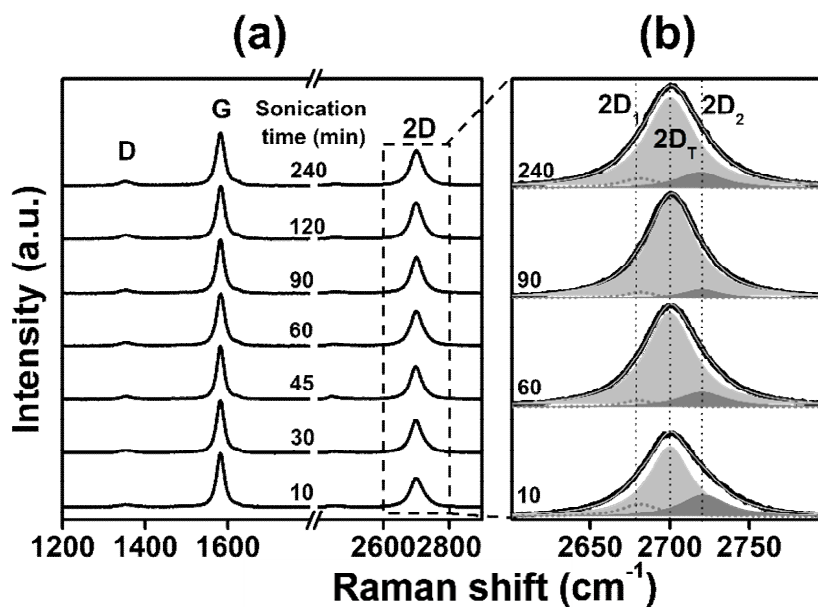


Figure 4.4.1 Raman spectra(a) and 2D peak deconvolution(b) with varying sonication time of GO precursor

More specifically, we investigated the effect of precursor on transformation from incommensurate turbostratic stacking into commensurate AB-stacking. The portion of the AB-stacking (graphitic) domain in rGO film strongly depends on the sonication time for GO hydrogel used for coating.

The graphitic portion of rGO film was measured by deconvolution analysis of Raman 2D peak as in the temperature effect analysis. (Figure 4.4.1) Two peaks at the center of $\sim 2680\text{ cm}^{-1}$ and $\sim 2720\text{ cm}^{-1}$ are denoted as 2D₁ and 2D₂ peak (dark gray). The peak at the center of $\sim 2700\text{ cm}^{-1}$ is denoted as the 2D_T peak (gray). The sum of the fitting curves (light gray solid line) follows the raw data (black solid line) well. When looking at the trend of the Raman spectrum, two characteristic trends were observed. The D peak tended to increase with the sonication time, and the 2D peak was observed to transition

from the asymmetric peak to the symmetric peak. The increase in D peak indicates that the defect in the rGO layer increased, and this is probably due to the edge created as the size of the GO nanosheets decreases with the sonication time. Meanwhile, the change of the 2D peak from asymmetric to symmetric is related to the 3D ordering between the layers of the rGO, suggesting that the AB-stacking domain decreases and the ratio of the turbostratic stacking domain increase with the sonication time. For more quantitative analysis, the process of measuring the area of each peak and deconvolution of the Raman 2D peak is required.

We should note that when the AB-stacking portion is small (<40%), the asymmetry of the Raman 2D peak is not prominent, so the deconvolution analysis has some ambiguity. For example, there were researches, in which, although these nearly symmetric Raman 2D peaks can be fitted by the only single turbostratic stacking domain peak, the non-negligible portion of the AB-stacking region is observed by XRD, TEM, and electron diffraction.^{60,96} On the other hand, even if there is no prominent asymmetry in the 2D peak, it is possible to deconvolute the peak into three peaks. In this case, a significant portion of AB-stacking order is estimated by deconvolution of nearly symmetric 2D peak obtain from <2000°C annealed rGO film.⁹⁷ We also experienced similar ambiguity that the R-square of all spectra were higher than 0.99 even with single peak fitting, but it was supported by the following evidence (see below) that the triple peak fitting was more accurate than single peak fitting. Firstly, the 2D peak position converged from 2704 cm^{-1} to 2700 cm^{-1} , the 2D peak position of the well-known turbostratic graphite, with increasing sonication time (Figure 4.4.2)

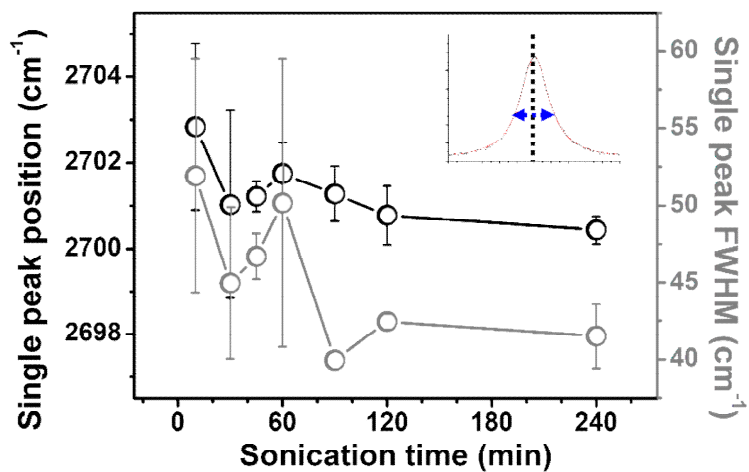


Figure 4.4.2 Center position and FWHM of Raman 2D peak depending on the sonication time

$$R_a^2 = 1 - \frac{(n-1)(1-R^2)}{n-p-1}$$

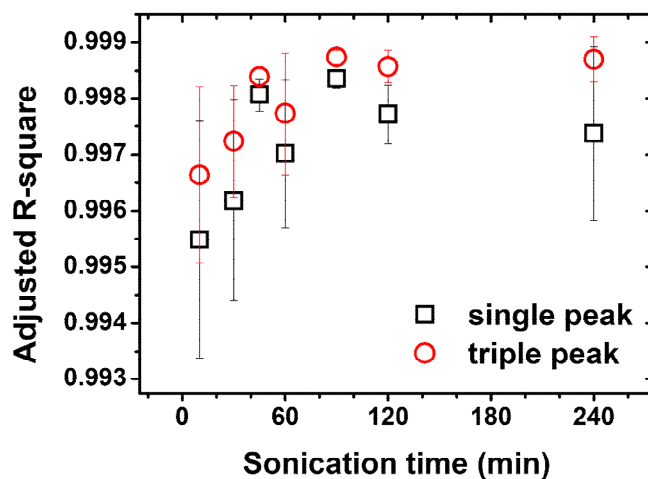


Figure 4.4.3 Comparison of adjusted R-square value of single peak fitting and triple peak fitting

Secondly, the adjusted R-square of triple peak fitting showed a higher value

than that of single peak fitting and again decreased when 5 peaks were assigned (Figure 4.4.3). Thirdly, the trend of graphitic portion decrease according to the sonication time observed through triple peak fitting coincided with the trend of XRD while single peak fitting gives a constant 0% regardless of sonication time (Figure 4.4.4 and Figure 4.4.5)

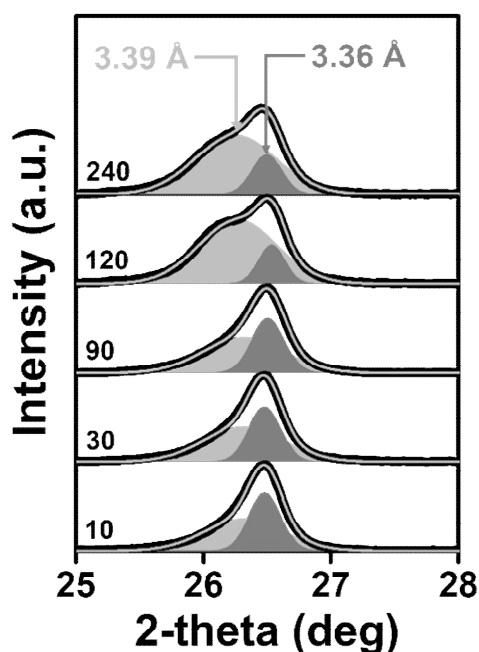


Figure 4.4.4 Deconvolution of the X-ray diffraction pattern from rGO film with varying sonication time

The graphitic portion of rGO film was found to be reduced rapidly with increasing sonication time and minimized at 90 min. The interlayer distance of the film is also measured to support this observation.⁹⁵ The interfacial structure of 1800°C annealed rGO film was investigated by X-ray diffraction (XRD) as shown in Figure 4.4.4. The large interlayer distance of GO film was greatly reduced after 1800°C annealing from ~ 8 Å to ~ 3.36 Å which

corresponds to the interlayer spacing of highly ordered pyrolytic graphite (HOPG). The drastic reduction of interlayer distance to 3.36 Å is mainly associated with the removal of intercalated water and oxygen-containing groups as observed in XPS data. Interestingly for all of the samples, shoulder peaks were observed at $d = 3.39$ Å, which means that our film is composed of two distinctive crystal domains with different 3D stacking order. As a result of analyzing the XRD pattern of rGO films made of GO hydrogels sonicated for different times, it was observed that the content of the crystal domain corresponding to 3.39 Å increased with the sonication time.

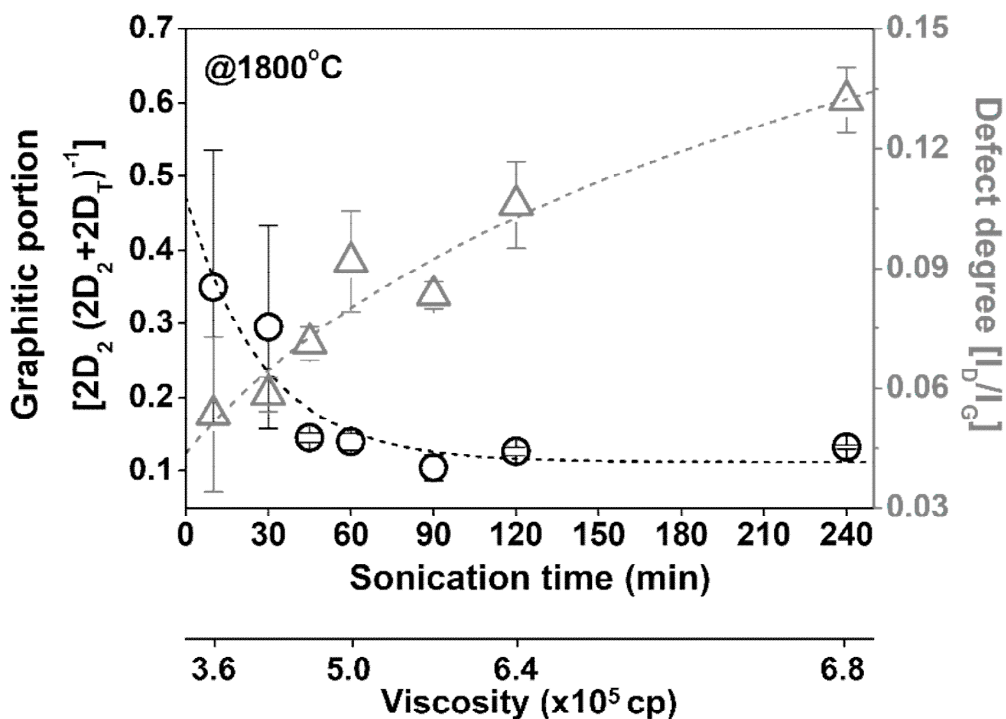


Figure 4.4.5 Degree of the defect and graphitic portion of rGO film depending on the sonication period of GO hydrogel

From a consistent trend with the Raman 2D spectra (Figure 4.4.5), it was confirmed that the XRD peak at 3.39 \AA is a crystal domain with a turbostratic stacking order. Besides the changes in stacking order, intralayer defects are increased with increasing sonication time. This is possibly due to the fragmentation of GO nanosheets during sonication, which increases the number of edges in the final rGO film.²⁸

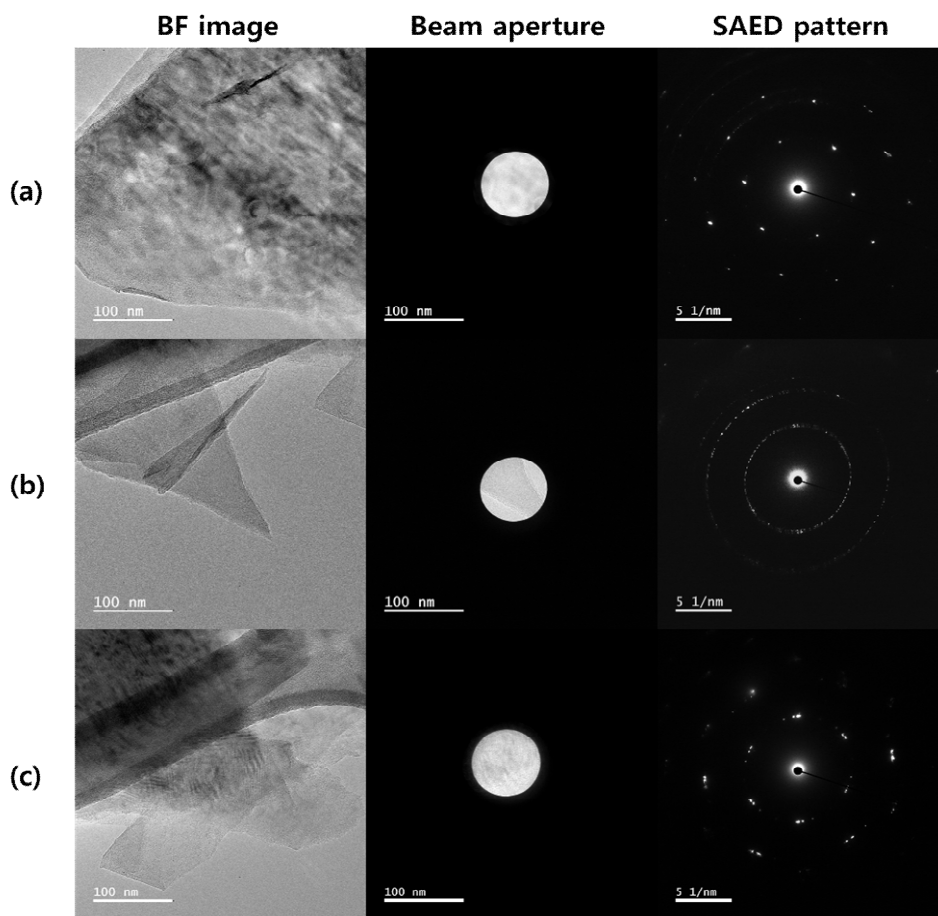


Figure 4.4.6 TEM images and selected area electron diffraction pattern of rGO flake from rGO film (90 min, 1800°C). AB-stacking region (a), turbostratic stacking region (b), (c).

In addition, TEM imaging and selected area electron diffraction experiments were performed on the rGO film to directly observe the mixed stacking order of the rGO film. To put it on the TEM grid, the rGO film was again immersed in water and sonicated for a certain period of time. The rGO flake colloid re-peeled in this way was dried by drop cast on the lacey carbon TEM grid. TEM and SAED experiments were performed at 80kV beam voltage to minimize damage caused by the beam of the sample. Moire fringe was observed in the part where AB-stacking was formed, and it was confirmed that the electron diffraction pattern in the part had a hexagonal pattern of AB-stacking. On the other hand, in most of the particles, a ring pattern or a twisted hexagonal pattern was observed in the region where the fringe did not appear. Therefore, in addition to the indirect quantitative measurement method using Raman, we observed the mixed stacking order of our rGO film through direct qualitative measurement using TEM.

4.5 Stacking-order driven electrical properties of rGO film

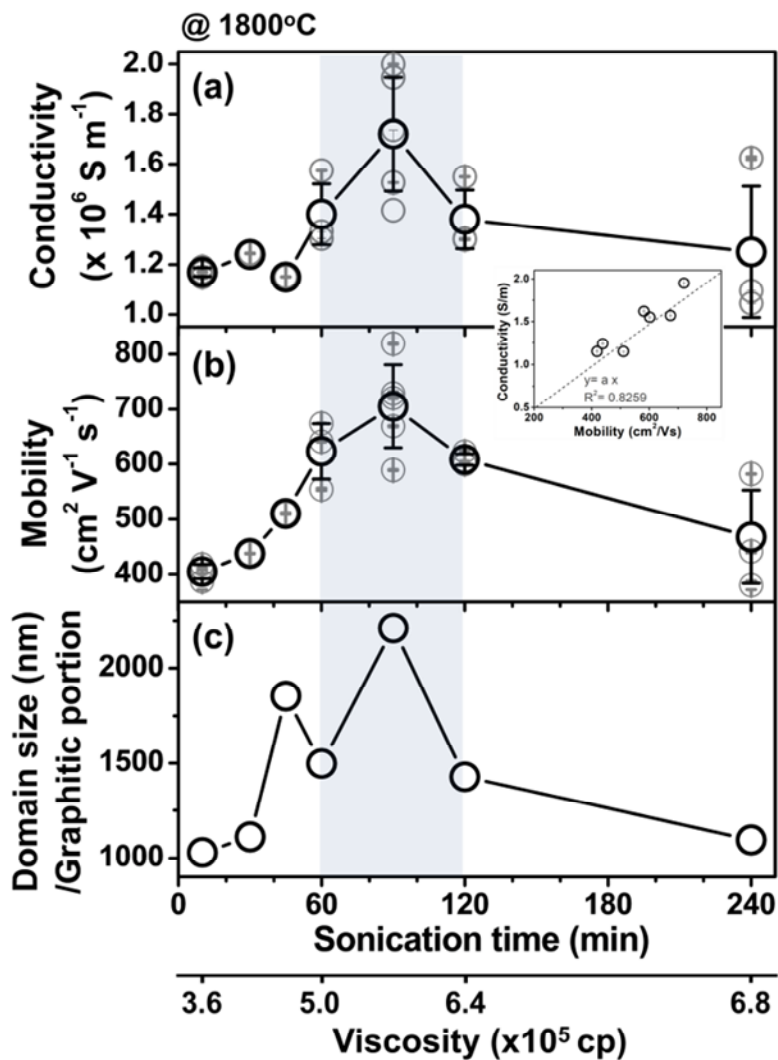


Figure 4.5.1 Maximization of electrical properties by an interplay between defect and stacking order (a) in-plane electrical conductivity of rGO film with varying sonication time of GO hydrogel measured by Van der Pauw method.

(b) the in-plane carrier mobility of rGO film with varying sonication time of GO hydrogel measured by Hall measurement system. (c) Inverse product of $2D_2/(2D_2 + 2D_T)$ and I_D/I_G depending on the sonication time of GO hydrogel were calculated from Figure 2e. Range of optimized conductivity, mobility, and structural parameters are marked as a shaded region. Gray circles in (a) and (b) represent each sample measurements with an error bar denoting standard deviation of three independent measurements

So far, we have seen how the chemistry and structure of rGO films change through the structural engineering of precursors using sonication. To study the effect of stacking structure on electrical properties of macroscopic rGO film, conductivity, mobility, and carrier density of rGO film made from GO precursor sonicated for the different period were investigated. The in-plane electrical conductivity and Hall mobility of 1800°C-reduced graphene oxide film were determined by a Van der Pauw method and are shown in Figure 4.4.1 (a) and Figure 4.4.1 (b) respectively. Figure 4.4.1 (a) shows the longitudinal conductivity with varying sonication time of GO hydrogel. The measurements were calibrated by the standard sample (ITO) given by the manufacturer. Varying the sonication time, a sharp increase up to 90 minutes, and a continuous decrease after 90 minutes was observed.

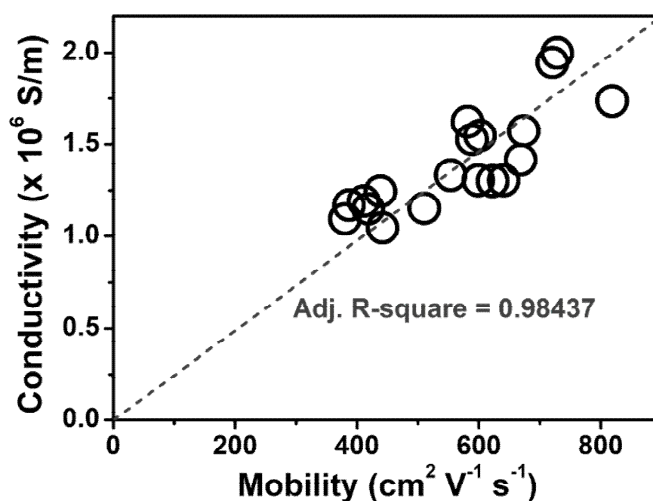
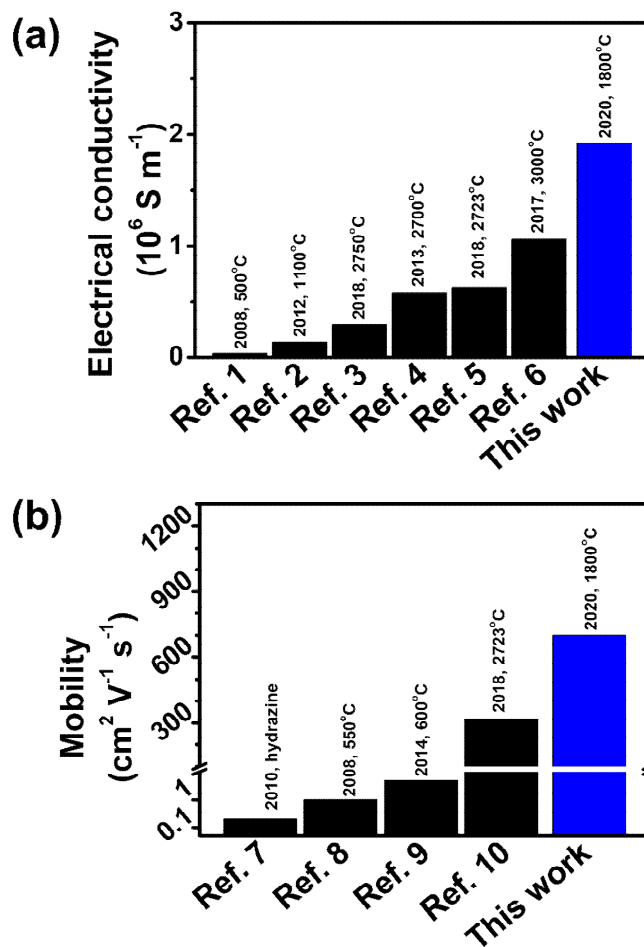


Figure 4.5.2 Linear correlation between mobility and conductivity

Mobility over sonication time was also found to follow the trend, and it was observed that conductivity and mobility had a linear relationship (Figure 4.4.2). From the Drude model ($\sigma = ne\mu$), this observation suggests that the mobility of the film changes dominantly rather than the carrier density with varying the sonication time of GO hydrogel. Carrier density of rGO film is mainly determined by residual oxygen contaminants which were almost fully removed after 1800°C annealing (Section 4.3). So, the variation of conductivity with different sonication periods of GO hydrogel is mainly due to variation of mobility.



Reference1 | Chen, H., et al. (2008). *Advanced Materials* 20(18): 3557-3561.
Reference2 | Lin, X., et al. (2012). *ACS nano* 6(12): 10708-10719.
Reference3 | Chen, X., et al. (2018). *Carbon* 132: 294-303.
Reference4 | Rozada, R., et al. (2013). *Nano Research* 6(3): 216.
Reference5 | Wang, Y., et al. (2018). *Materials Today* 21(2): 186-192.
Reference6 | Peng, L., et al. (2017). *Advanced Materials* 29(27).
Reference7 | Kobayashi, T., et al. (2010). *Small* 6(11): 1210-1215.
Reference8 | Eda, G., et al. (2008). *Nat Nano* 3(5): 270-274.
Reference9 | Negishi, R. and Y. Kobayashi (2014). *Applied Physics Letters* 105(25): 253502.
Reference10 | Wang, Y., et al. (2018). *Materials Today* 21(2): 186-192.

Figure 4.5.3 Comparison of electrical conductivity and mobility with previous researches

To the best of our knowledge, the maximum electrical conductivity and mobility of rGO film achieved is record value among existing pristine graphene film (Figure 4.4.3). Until now, rGO free-standing film has remained at a level similar to or lower than that of commercial pyrolytic graphite or HOPG. However, we were able to achieve electrical conductivity beyond these by adjusting the stacking order while maintaining the temperature appropriately. The ultrahigh electrical conductivity and mobility are attributed to the unique structural characteristic of our rGO film, near-perfect in-plane crystallinity with highly turbostratic stacking order (Figure 4.4.4).

It is interesting to find the product of the domain size and inverse of graphitic portion have the same trend with mobility (Figure 4.4.1 (c)) Mobility of the semiconducting material can be described by $\mu = \frac{e\tau}{m^*}$. In the classical point of view, the scattering time of the carriers traveling through the film can be simplified as a domain size divided by fermi-velocity. Domain size (L_a) of the film can be roughly estimated by Cancado's empirical formula ($L_a = 2.4 * 10^{-10} \lambda^4 \left(\frac{I_D}{I_G}\right)^{-1}$). With just naive thought, the larger the graphitic portion, the larger the average effective mass of the entire film is expected. Therefore, mobility can be expected to be proportional to the domain size while it is inverse proportional to the portion of the AB-stacking region. Therefore, in this low defect regime, it was confirmed that not only the defect density but also the stacking order have a great influence on carrier mobility and conductivity as shown in figure 4.4.1.

Recently, for few-layer graphene, there has been a lot of experimental evidence that turbostratic stacking graphene is superior to AB stacking

graphene. AB-stacked graphene has a finite effective mass ($\approx 0.3m_e$) derived from the parabolic band structure, while the carriers in SLG are massless. Fermi velocity of turbostratic stacking graphene was found to exceed that of AB-stacking graphene and even single-layer graphene on SiO₂ substrate. Lucian et al. report increments in the Fermi velocity in bilayer graphene by increasing twist angles and finally it becomes to be similar to that of SLG for twist angles larger than 5°. ⁹⁸ We expect a similar phenomenon will take place in highly restored free-standing rGO film which can be regarded as multilayer graphene with a tremendous number of layers. This can explain why turbostratic stacking rGO film possesses higher mobility than AB-stacking rGO film.

4.6 Thermal expansion assisted hot pressing

To see the possibility of stressed graphitization suggested in previous researches, we also designed the tungsten-graphite-based hot pressing jig. The pressure induced by thermal expansion have its own merit that the pressure is invariant with the pressing area in principle. Here the GO film is sandwiched by graphite plates which are tightened by W blocks and bolts. Order of ~ 10 MPa are found to be generated inside the jig according to the numerical simulation because the thermal expansion coefficient of graphite is larger than the outer W holder. The pressure applied could be controlled by the position of bolts and the thickness of the graphite/tungsten block. The maximum pressure we can apply is determined by the stuck phenomenon between graphite and graphene films, which makes delamination without damaging film difficult.

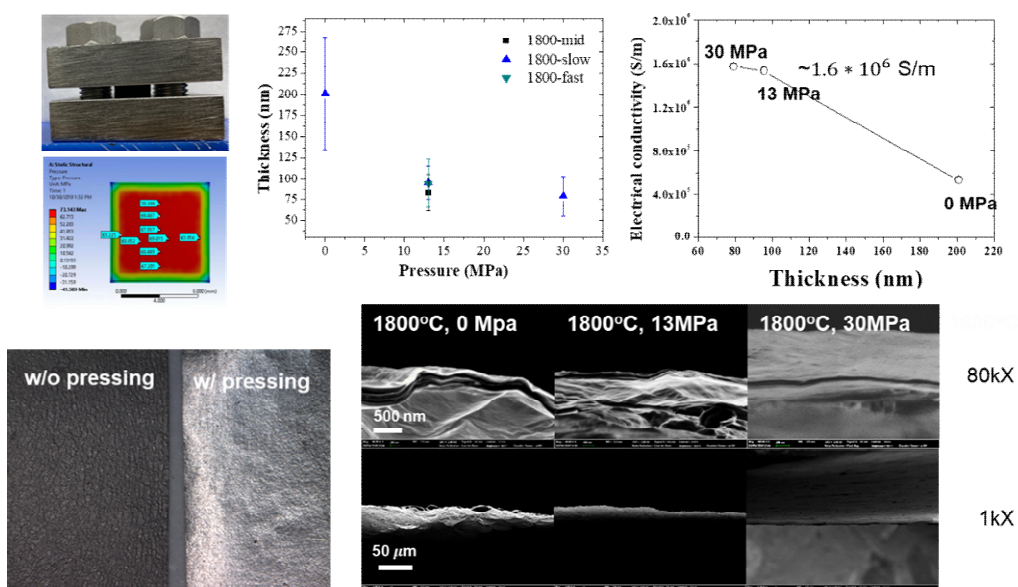


Figure 4.6.1 Designed hot press jig based on W and graphite. Thickness

depending on the pressure and heating rate. Electrical conductivity depending on pressure at 1800°C annealing. Optical and SEM image with different pressing conditions

As pressure increases dramatic removal of micropores and wrinkles was observed, which results in the decrease of average thicknesses and the increase of electrical conductivity.

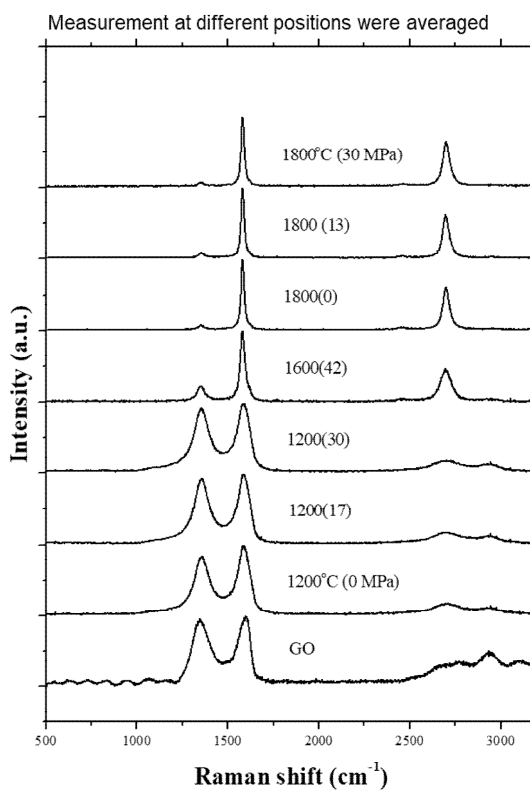


Figure 4.6.2 Raman spectra of graphene film with different annealing temperature and pressure

We also expected a higher degree of restoration when pressure is applied. To confirm our hypothesis, we've measured the Raman spectroscopy of graphene films annealed at different conditions. As expected, the D peak

decreases with increasing temperature. However, with increasing pressure, there were no pronounced differences. This is possibly due to not enough pressure limited by the stuck problem.

Chapter 5

Summary and Conclusion

A new method of engineering the stacking order was proposed, and for the first time, the relationship between the conductivity and the stacking order of rGO film was experimentally shown to achieve record conductivity. Macroscopic films consisting of stacked graphene are prepared using sonication-assisted binder-free graphene oxide (GO) hydrogel as a precursor. We engineered the stacking order of rGO film by engineering GO film precursor by sonication of GO hydrogel and we studied the stacking-order-driven electrical properties of rGO film. After heat treatment up to 1800°C, the resulting reduced graphene oxide (rGO) freestanding film has highly restored in-plane crystallinity while turbostratic stacking order is almost retained. The role of the sonication process for engineering rGO film stacking order is understood by two-fold, full exfoliation of graphite oxide and gelation. The degree of cross-linking is increased by sonication of the GO dispersion, which possibly suppresses the relative motion of flakes during annealing. This rationally designed precursor leads to an increase in the portion of the turbostratic stacking region in the rGO film. Electrical conductivity and mobility were maximized via the interplay of stacking order and defects. The weaker interaction between neighboring graphene layers in turbostratic stacking graphene can significantly decrease the effective mass of electrons traveling through the film. The optimized film turns out to possess record-high conductivity ($1.95 \times 10^6 \text{ S m}^{-1}$) and record-high mobility ($720 \text{ cm}^2 \text{ V}^{-1} \text{ s}^{-1}$). Such an rGO film with optimized structures and properties shows great potentials in EMI shielding and high-power electronics.

Bibliography

- 1 Novoselov, K. S. & Geim, A. The rise of graphene. *Nat. Mater* **6**, 183-191 (2007).
- 2 Novoselov, K. S. *et al.* Electric field effect in atomically thin carbon films. *science* **306**, 666-669 (2004).
- 3 Lee, C., Wei, X., Kysar, J. W. & Hone, J. Measurement of the elastic properties and intrinsic strength of monolayer graphene. *science* **321**, 385-388 (2008).
- 4 Novoselov, K. S. *et al.* A roadmap for graphene. *nature* **490**, 192-200 (2012).
- 5 Coroş, M., Pogăcean, F., Măgeruşan, L., Socaci, C. & Pruneanu, S. A brief overview on synthesis and applications of graphene and graphene-based nanomaterials. *Frontiers of Materials Science* **13**, 23-32 (2019).
- 6 Ren, S., Rong, P. & Yu, Q. Preparations, properties and applications of graphene in functional devices: A concise review. *Ceramics International* **44**, 11940-11955 (2018).
- 7 Aissa, B., Memon, N. K., Ali, A. & Khraisheh, M. K. Recent progress in the growth and applications of graphene as a smart material: A review. *Frontiers in Materials* **2**, 58 (2015).
- 8 Lee, H. C. *et al.* Review of the synthesis, transfer, characterization and growth mechanisms of single and multilayer graphene. *RSC advances* **7**, 15644-15693 (2017).
- 9 Dideikin, A. T. & Vul, A. Y. Graphene oxide and derivatives: the place in graphene family. *Frontiers in Physics* **6**, 149 (2019).
- 10 Dikin, D. A. *et al.* Preparation and characterization of graphene oxide paper. *Nature* **448**, 457 (2007).
- 11 Marcano, D. C. *et al.* Improved synthesis of graphene oxide. *ACS nano* **4**, 4806-4814 (2010).
- 12 Morimoto, N. *et al.* Real-Time, in Situ Monitoring of the Oxidation of Graphite: Lessons Learned. *Chemistry of Materials* **29**, 2150-2156 (2017).
- 13 Lerf, A., He, H., Forster, M. & Klinowski, J. Structure of graphite oxide revisited.

- The Journal of Physical Chemistry B* **102**, 4477-4482 (1998).
- 14 Mkhoyan, K. A. *et al.* Atomic and electronic structure of graphene-oxide. *Nano letters* **9**, 1058-1063 (2009).
 - 15 Li, D., Muller, M. B., Gilje, S., Kaner, R. B. & Wallace, G. G. Processable aqueous dispersions of graphene nanosheets. *Nat Nano* **3**, 101-105, (2008).
 - 16 Erickson, K. *et al.* Determination of the local chemical structure of graphene oxide and reduced graphene oxide. *Advanced Materials* **22**, 4467-4472 (2010).
 - 17 Gómez-Navarro, C. *et al.* Atomic structure of reduced graphene oxide. *Nano letters* **10**, 1144-1148 (2010).
 - 18 Pei, S. & Cheng, H.-M. The reduction of graphene oxide. *Carbon* **50**, 3210-3228 (2012).
 - 19 Singh, R. K., Kumar, R. & Singh, D. P. Graphene oxide: strategies for synthesis, reduction and frontier applications. *RSC Advances* **6**, 64993-65011 (2016).
 - 20 Pei, S., Zhao, J., Du, J., Ren, W. & Cheng, H.-M. Direct reduction of graphene oxide films into highly conductive and flexible graphene films by hydrohalic acids. *Carbon* **48**, 4466-4474 (2010).
 - 21 Cong, H. P., Chen, J. F. & Yu, S. H. Graphene-based macroscopic assemblies and architectures: An emerging material system. *Chemical Society Reviews* **43**, 7295-7325, doi:10.1039/c4cs00181h (2014).
 - 22 Li, Z., Liu, Z., Sun, H. & Gao, C. Superstructured Assembly of Nanocarbons: Fullerenes, Nanotubes, and Graphene. *Chemical Reviews* **115**, 7046-7117, doi:10.1021/acs.chemrev.5b00102 (2015).
 - 23 Chen, Y. *et al.* Reduced Graphene Oxide Films with Ultrahigh Conductivity as Li-Ion Battery Current Collectors. *Nano Letters* **16**, 3616-3623 (2016).
 - 24 Shahzad, F. *et al.* Electromagnetic interference shielding with 2D transition metal carbides (MXenes). *Science* **353**, 1137-1140 (2016).
 - 25 Shen, B., Zhai, W. & Zheng, W. Ultrathin Flexible Graphene Film: An Excellent Thermal Conducting Material with Efficient EMI Shielding. *Advanced Functional Materials* **24**, 4542-4548 (2014).
 - 26 Xin, G. *et al.* Large-Area Freestanding Graphene Paper for Superior Thermal Management. *Advanced Materials* **26**, 4521-4526 (2014).
 - 27 Ding, J. *et al.* Hydroxylated graphene-based flexible carbon film with ultrahigh

- electrical and thermal conductivity. *Nanotechnology* **28**, 39LT01 (2017).
- 28 Peng, L. *et al.* Ultrahigh Thermal Conductive yet Superflexible Graphene Films. *Advanced Materials* **29** (2017).
- 29 Teng, C. *et al.* Ultrahigh Conductive Graphene Paper Based on Ball-Milling Exfoliated Graphene. *Advanced Functional Materials* **27**, 1700240 (2017).
- 30 Liu, L., Wang, Y., Li, G., Qin, S. & Zhang, T. Ultrathin free-standing graphene oxide film based flexible touchless sensor. *Journal of Semiconductors* **39**, 013002 (2018).
- 31 Konios, D., Stylianakis, M. M., Stratakis, E. & Kymakis, E. Dispersion behaviour of graphene oxide and reduced graphene oxide. *Journal of Colloid and Interface Science* **430**, 108-112 (2014).
- 32 Chen, C. *et al.* Self-Assembled Free-Standing Graphite Oxide Membrane. *Advanced Materials* **21**, 3007-3011 (2009).
- 33 Liu, Z. *et al.* Wet-Spun Continuous Graphene Films. *Chemistry of Materials* **26**, 6786-6795, doi:10.1021/cm5033089 (2014).
- 34 Zhang, M. *et al.* Multifunctional Pristine Chemically Modified Graphene Films as Strong as Stainless Steel. *Advanced Materials* **27**, 6708-6713, doi:10.1002/adma.201503045 (2015).
- 35 Wei, Q. *et al.* Superhigh Electromagnetic Interference Shielding of Ultrathin Aligned Pristine Graphene Nanosheets Film. *Advanced Materials* **32**, 1907411 (2020).
- 36 Zhong, J. *et al.* Efficient and scalable synthesis of highly aligned and compact two-dimensional nanosheet films with record performances. *Nature communications* **9**, 3484 (2018).
- 37 Kasap, S., Koughia, C. & Ruda, H. E. in *Springer Handbook of Electronic and Photonic Materials* 1-1 (Springer, 2017).
- 38 Mattevi, C. *et al.* Evolution of electrical, chemical, and structural properties of transparent and conducting chemically derived graphene thin films. *Advanced Functional Materials* **19**, 2577-2583 (2009).
- 39 Hass, J. *et al.* Why multilayer graphene on 4 H- SiC (000 1) behaves like a single sheet of graphene. *Physical Review Letters* **100**, 125504 (2008).
- 40 Shallcross, S., Sharma, S., Kandelaki, E. & Pankratov, O. Electronic structure of

- turbostratic graphene. *Physical Review B* **81**, 165105 (2010).
- 41 Wu, X. *et al.* Boosting carrier mobility of synthetic few layer graphene on SiO₂ by interlayer rotation and decoupling. *Advanced Materials Interfaces* **5**, 1800454 (2018).
 - 42 Mogera, U. & Kulkarni, G. U. A new twist in graphene research: Twisted graphene. *Carbon* **156**, 470-487 (2020).
 - 43 Bolotin, K. I. *et al.* Ultrahigh electron mobility in suspended graphene. *Solid State Communications* **146**, 351-355 (2008).
 - 44 Zhao, S. *et al.* Graphene-based free-standing bendable films: designs, fabrications, and applications. *Materials Today Advances* **6**, 100060 (2020).
 - 45 Yao, Y. & Ping, J. Recent advances in graphene-based freestanding paper-like materials for sensing applications. *TrAC Trends in Analytical Chemistry* (2018).
 - 46 Wan, S., Peng, J., Jiang, L. & Cheng, Q. Bioinspired Graphene-Based Nanocomposites and Their Application in Flexible Energy Devices. *Advanced Materials* **28**, 7862-7898 (2016).
 - 47 Du, X., Skachko, I., Barker, A. & Andrei, E. Y. Approaching ballistic transport in suspended graphene. *Nature nanotechnology* **3**, 491-495 (2008).
 - 48 Chen, J.-H. *et al.* Charged-impurity scattering in graphene. *Nature physics* **4**, 377-381 (2008).
 - 49 Chen, J.-H., Cullen, W. G., Jang, C., Fuhrer, M. & Williams, E. D. Defect scattering in graphene. *Physical review letters* **102**, 236805 (2009).
 - 50 Yu, Q. *et al.* Control and characterization of individual grains and grain boundaries in graphene grown by chemical vapour deposition. *Nature materials* **10**, 443-449 (2011).
 - 51 Kobayashi, T., Kimura, N., Chi, J., Hirata, S. & Hobar, D. Channel-length-dependent field-effect mobility and carrier concentration of reduced graphene oxide thin-film transistors. *Small* **6**, 1210-1215 (2010).
 - 52 Negishi, R. & Kobayashi, Y. Extraordinary suppression of carrier scattering in large area graphene oxide films. *Applied Physics Letters* **105**, 253502 (2014).
 - 53 Rozada, R. *et al.* Towards full repair of defects in reduced graphene oxide films by two-step graphitization. *Nano Research* **6**, 216 (2013).
 - 54 Xin, G., Zhu, W., Yao, T., Scott, S. M. & Lian, J. Microstructure control of

- macroscopic graphene paper by electrospray deposition and its effect on thermal and electrical conductivities. *Applied Physics Letters* **110**, 091909 (2017).
- 55 Lin, X. *et al.* Fabrication of highly-aligned, conductive, and strong graphene papers using ultralarge graphene oxide sheets. *ACS nano* **6**, 10708-10719 (2012).
- 56 Xin, G. *et al.* Highly thermally conductive and mechanically strong graphene fibers. *Science* **349**, 1083-1087 (2015).
- 57 Xu, Z., Sun, H., Zhao, X. & Gao, C. Ultrastrong fibers assembled from giant graphene oxide sheets. *Advanced Materials* **25**, 188-193 (2013).
- 58 Dong, L., Yang, J., Chhowalla, M. & Loh, K. P. Synthesis and reduction of large sized graphene oxide sheets. *Chemical Society Reviews* **46**, 7306-7316 (2017).
- 59 Wang, B. *et al.* Ultrastiff, Strong, and Highly Thermally Conductive Crystalline Graphitic Films with Mixed Stacking Order. *Advanced Materials*, 1903039 (2019).
- 60 Chen, X. *et al.* Graphitization of graphene oxide films under pressure. *Carbon* **132**, 294-303 (2018).
- 61 Zhang, M., Huang, L., Chen, J., Li, C. & Shi, G. Ultratough, Ultrastrong, and Highly Conductive Graphene Films with Arbitrary Sizes. *Advanced Materials* **26**, 7588-7592 (2014).
- 62 Wen, Y., Wu, M., Zhang, M., Li, C. & Shi, G. Topological design of ultrastrong and highly conductive graphene films. *Advanced Materials* **29**, 1702831 (2017).
- 63 Wan, S., Fang, S., Jiang, L., Cheng, Q. & Baughman, R. H. Strong, Conductive, Foldable Graphene Sheets by Sequential Ionic and π Bridging. *Advanced Materials* **30**, 1802733 (2018).
- 64 Wan, S. *et al.* Ultrastrong Graphene Films via Long-Chain π -Bridging. *Matter* (2019).
- 65 Eigler, S. *et al.* Wet chemical synthesis of graphene. *Advanced materials* **25**, 3583-3587 (2013).
- 66 Uemura, K., Ikuta, T. & Maehashi, K. Turbostratic stacked CVD graphene for high-performance devices. *Japanese Journal of Applied Physics* **57**, 030311 (2018).

- 67 Jin, S. *et al.* Ultrahigh Strength and Modulus Graphene-Based Hybrid Carbons with AB-Stacked and Turbostratic Structures. *Advanced Functional Materials*, 2005381 (2020).
- 68 Wang, N. *et al.* Tailoring the thermal and mechanical properties of graphene film by structural engineering. *Small* **14**, 1801346 (2018).
- 69 Murata, H., Saitoh, N., Yoshizawa, N., Suemasu, T. & Toko, K. High-quality multilayer graphene on an insulator formed by diffusion controlled Ni-induced layer exchange. *Applied Physics Letters* **111**, 243104 (2017).
- 70 Ta, H. Q. *et al.* Stranski–Krastanov and Volmer–Weber CVD growth regimes to control the stacking order in bilayer graphene. *Nano letters* **16**, 6403-6410 (2016).
- 71 Wang, B. *et al.* Controlled folding of single crystal graphene. *Nano letters* **17**, 1467-1473 (2017).
- 72 Wei, C. *et al.* Turbostratic multilayer graphene synthesis on CVD graphene template toward improving electrical performance. *Japanese Journal of Applied Physics* **58**, S11B04 (2019).
- 73 Negishi, R. *et al.* Turbostratic stacking effect in multilayer graphene on the electrical transport properties. *physica status solidi (b)* **257**, 1900437 (2020).
- 74 Akbari, A. *et al.* Large-area graphene-based nanofiltration membranes by shear alignment of discotic nematic liquid crystals of graphene oxide. *Nature communications* **7**, 10891 (2016).
- 75 Li, C. & Shi, G. Functional Gels Based on Chemically Modified Graphenes. *Advanced Materials* **26**, 3992-4012 (2014).
- 76 Compton, O. C. *et al.* Additive-free hydrogelation of graphene oxide by ultrasonication. *Carbon* **50**, 3399-3406 (2012).
- 77 Ibrahim, K. H. *et al.* A Novel Femtosecond Laser-Assisted Method for the Synthesis of Reduced Graphene Oxide Gels and Thin Films with Tunable Properties. *Advanced Materials Interfaces* **3** (2016).
- 78 Lebedeva, I. V. *et al.* Fast diffusion of a graphene flake on a graphene layer. *Physical Review B* **82**, 155460 (2010).
- 79 Mellado, C., Figueroa, T., Baez, R., Melendrez, M. & Fernandez, K. Effects of probe and bath ultrasonic treatments on graphene oxide structure. *Materials*

- Today Chemistry* **13**, 1-7 (2019).
- 80 McAllister, M. J. *et al.* Single Sheet Functionalized Graphene by Oxidation and Thermal Expansion of Graphite. *Chemistry of Materials* **19**, 4396-4404 (2007).
- 81 Konkena, B. & Vasudevan, S. Glass, gel, and liquid crystals: arrested states of graphene oxide aqueous dispersions. *The Journal of Physical Chemistry C* **118**, 21706-21713 (2014).
- 82 Buchsteiner, A., Lerf, A. & Pieper, J. Water Dynamics in Graphite Oxide Investigated with Neutron Scattering. *The Journal of Physical Chemistry B* **110**, 22328-22338 (2006).
- 83 Lerf, A. *et al.* Hydration behavior and dynamics of water molecules in graphite oxide. *Journal of Physics and Chemistry of Solids* **67**, 1106-1110 (2006).
- 84 Cerveny, S., Barroso-Bujans, F., Alegria, A. & Colmenero, J. Dynamics of water intercalated in graphite oxide. *The Journal of Physical Chemistry C* **114**, 2604-2612 (2010).
- 85 Jeong, H.-K. *et al.* Evidence of Graphitic AB Stacking Order of Graphite Oxides. *Journal of the American Chemical Society* **130**, 1362-1366 (2008).
- 86 Ye, S. & Feng, J. The effect of sonication treatment of graphene oxide on the mechanical properties of the assembled films. *RSC Advances* **6**, 39681-39687 (2016).
- 87 Cai, W. *et al.* Synthesis and solid-state NMR structural characterization of ¹³C-labeled graphite oxide. *Science* **321**, 1815-1817 (2008).
- 88 Szabó, T., Berkesi, O. & Dékány, I. DRIFT study of deuterium-exchanged graphite oxide. *Carbon* **43**, 3186-3189 (2005).
- 89 Cançado, L. *et al.* General equation for the determination of the crystallite size L_a of nanographite by Raman spectroscopy. *Applied Physics Letters* **88**, 163106 (2006).
- 90 Díez-Betriu, X. *et al.* Raman spectroscopy for the study of reduction mechanisms and optimization of conductivity in graphene oxide thin films. *Journal of Materials Chemistry C* **1**, 6905-6912 (2013).
- 91 Cançado, L. G. *et al.* Quantifying defects in graphene via Raman spectroscopy at different excitation energies. *Nano letters* **11**, 3190-3196 (2011).
- 92 Cançado, L. G. *et al.* Disentangling contributions of point and line defects in

- the Raman spectra of graphene-related materials. *2D Materials* **4**, 025039 (2017).
- 93 Jin, M. *et al.* Facile physical route to highly crystalline graphene. *Advanced Functional Materials* **21**, 3496-3501 (2011).
- 94 Rozada, R. *et al.* From graphene oxide to pristine graphene: revealing the inner workings of the full structural restoration. *Nanoscale* **7**, 2374-2390 (2015).
- 95 Malard, L. M., Pimenta, M. A., Dresselhaus, G. & Dresselhaus, M. S. Raman spectroscopy in graphene. *Physics Reports* **473**, 51-87 (2009).
- 96 Song, L. *et al.* Effect of high-temperature thermal treatment on the structure and adsorption properties of reduced graphene oxide. *Carbon* **52**, 608-612 (2013).
- 97 Ishida, T., Miyata, Y., Shinoda, Y. & Kobayashi, Y. Anomalous restoration of graphitic layers from graphene oxide in ethanol environment at ultrahigh temperature using solar furnace. *Applied Physics Express* **9**, 025103 (2016).
- 98 Luican, A. *et al.* Single-layer behavior and its breakdown in twisted graphene layers. *Physical review letters* **106**, 126802 (2011).

초록

본 연구에서는 독립된 환원그래핀옥사이드 필름의 구조와 전기적 특성간의 관계에 대한 실험적 연구를 수행하였으며, 높은 전기전도도와 전하 이동도를 가지는 환원그래핀옥사이드 필름의 합성방법이 개발되었다. 높은 전기전도도를 가지는 탄소 기반 독립형 필름에 대한 지속적인 요구에도 불구하고 기존 환원그래핀옥사이드 필름의 전기전도도는 고도로 정렬된 열분해 흑연 (HOPG)의 전기전도도 이하로 제한되는 실정이었다. 이는 전하의 산란을 유발하는 그래핀 평면 내 결함의 존재와 산소 및 결함의 제거 과정에서 동반되는 삼차원 정렬, 즉 흑연화에 의한 한계였다. 1500도 이상의 열적 가열을 통해 평면 내 결함과 산소는 상당한 수준으로 제거될 수 있으나 각 층간에서도 정렬이 일어나면서 무작위-배열구조 (turbostratic stacking order)가 점차 AB-배열구조(AB-stacking order)로 열적 변환된다는 많은 실험적 선행 연구가 있었다. 전기적 성질의 관점에서 봤을 때, 이는 그래핀의 선형 밴드구조를 포물선 밴드구조로 변화시킴으로서 유효질량을 높이고 페르미 속도를 낮출 가능성이 있다. 따라서 평면 내 결함을 치유하면서도 AB-배열구조의 형성을 억제하는 합성 방법에 대한 연구가 필요하다.

본 연구에서는 기록적으로 높은 전기전도도와 운반자 이동도를 가진 독립된 환원그래핀옥사이드 필름의 합성 방법이 보고되었다. 이 독립된 환원그래핀옥사이드 필름은 고도로 복원된 평면 내 결정성을 가지면서도 무작위 배열구조가 거의 유지되는 구조를 가지고 있다. 필름은 1800°C 에서 별도의 첨가물이 없는 그래핀옥사이드 하이드로겔 필름을 어닐링하여 합성되었다. AB-배열구조의 비율은 첨가제 없이 초음파 처리를 통해 얻어진 그래핀옥사이드 수용액의 겔화 과정을 통해 조절되었다. 조절 원리는 그래핀옥사이드 분산액 내의 박리되지 않은 입자들의 완전한 제거와, 그래핀옥사이드 하이드로겔에서 가교된 나노시트의 제한된 상대적인 움직임에 각각 초기 AB-배열 구조의 감소와 가열 도중 AB-배열 구조 형성의 감소를 유도하는 것으로 확인되었다. 필름은 기록적으로 높은 전기전도도 ($1.95 \text{ E}6 \text{ S m}^{-1}$) 와 기록적으로 높은 운반자 이동도 ($720 \text{ cm}^2 \text{ V}^{-1}$)

s^{-1}) 을 보유하는 것으로 드러났다.

이러한 필름의 우수한 전기적 특성은 적층 배열과 평면내 결합 정도 사이의 상호 최적화에 의해 달성되었다. 그래핀옥사이드의 초음파 처리과정에 따라서 결과되는 필름의 결합 정도는 점진적으로 증가함에도 불구하고 필름의 운반자 이동도는 증가하였는데, AB-배열구조의 감소 때문인 것을 확인하였다. 본 연구는 초고전도성 독립형 그래핀 필름을 제조하기 위한 비용 효율적이고 친환경적이며 확장 가능한 합성 방법을 제안하며, 미래의 고출력 또는 초고속 유연 전자 장치에 적용될 잠재력이 높다. 또한 본 연구에서 제시된 가교를 이용한 적층구조의 조절 개념은 그래핀 기반 필름 외의 다양한 반데르발스 물질에 적용될 수 있는 잠재력이 있다.

핵심어: 그래핀, 그래핀옥사이드, 환원그래핀옥사이드, 독립된 필름, 하이드로겔, 전기 전도도, 운반자 이동도, 결합, 적층 구조

학번: 2014-21342